Project No: 603502

DACCIWA

"Dynamics-aerosol-chemistry-cloud interactions in West Africa"

Deliverable

D3.5 Future Emissions

Due date of deliverable:	31/07/2018
Completion date of deliverable:	30/07/2018

Start date of DACCIWA project:	1st December 2013	**Project duration:**	60 months

Version:	[V1.0]
File name:	[D3.5_Future_Emissions_DACCIWA_v1.0.pdf]

Work Package Number:	3
Task Number:	5

Responsible partner for deliverable:	**ETHZ**
Contributing partners:	**UPMC, KIT, ETHZ, UoY**

Project coordinator name:	Prof. Dr. Peter Knippertz
Project coordinator organisation name:	Karlsruher Institut für Technologie

Dissemination level		
PU	Public	**x**
PP	Restricted to other programme participants (including the Commission Services)	
RE	Restricted to a group specified by the consortium (including the Commission Services)	
CO	Confidential, only for members of the consortium (including the Commission Services)	

Nature of Deliverable		
R	Report	**x**
P	Prototype	
D	Demonstrator	
O	Other	

Copyright

DOCUMENT INFO

Authors

Author	Beneficiary Short Name	E-Mail
Tanja Stanelle	ETHZ	tanja.stanelle@env.ethz.ch
Konrad Deetz	KIT	konrad.deetz@kit.edu
Bernhard Vogel	KIT	Bernhard.vogel@kit.edu
Mat Evans	UoY	mat.evans@york.ac.uk
Eleanor Morris	UoY	Eleanor.morris@york.ac.uk
Laurent Menut	UPMC	menut@lmd.polytechnique.fr

Changes with respect to the DoW

Issue	Comments

Dissemination and uptake

Target group addressed	Project internal / external
Scientific community	Internal and external

Document Control

Document version #	Date	Changes Made/Comments
0.1	14.05.2018	Template
0.2	29.06.2018	1st draft (send out to all authors)
0.3	12.07.2018	2nd draft (for approval by the general assembly)
1.0	30.07.2018	Final version approved by the general assembly

Table of Contents

1   Objectives of the report

Southern West Africa (SWA) is undergoing an unprecedented growth in population. It is expected that the population will continue to growth until the mid of this century. Increasing urbanisation and industrialisation is also forecasted. This region is one of the few places in the world, where an increase in anthropogenic emissions of non-CO_2 pollutants is expected until 2050. A change in aerosol concentration can impact the radiative budget via direct and indirect aerosol radiative forcing, which modifies the climate, but it also impacts the air quality. Small particles with diameter less than 2.5 µm (denoted PM2.5 in the following) can penetrate deeply into the lung, where they impair the lung function. Gases such as O_3 and NO_2 can also have adverse health impacts. To investigate how the air quality and the regional radiative forcing in Southern West Africa could involve until 2050 we performed sets of simulations with models covering the regional to the global scale.

The groups contributing to this deliverable use a range of model systems and follow different strategies for investigating the change in gas and aerosol distributions and their consequences for radiative forcing and air quality until 2050. The results of the studies will be presented from the finest to the coarsest resolutions.

The research group of the Karlsruhe Institute for Technology (KIT) addresses the question with their regional aerosol-atmosphere model COSMO-ART. They performed a process study focussing on aerosol impacts on clouds, radiation and the atmospheric dynamics over SWA. Therefore, they consider a clean, a polluted, and a reference case. The reference case reflects the conditions of 2nd – 3rd July 2016. The simulations are performed in a high horizontal resolution with a grid mesh of 2.5 km. The results of this study are presented in chapter 2.

In chapter 3 the team of the University Pierre and Marie Curie (UPMC) present their study with the regional WRF and CHIMERE model. The horizontal resolution of their model simulations was 60 km x 60 km. They performed offline simulations considering the time period 1st June – 30th September 2016. In the reference simulation they applied anthropogenic emission fluxes representative for the year 2016 and in a second simulation estimates for the year 2050.

The research group of the University of York used a global and regional offline chemistry model for their study. They performed global simulations with a horizontal resolution of 4° x 5°, and a regional grid mesh of about 0.25° x 0.3125°. They focussed on the year 2016, where a comprehensive measurement campaign took place in Southern West Africa during summer. They applied the emission inventory developed during the DACCIWA project for this time period. To determine the change in aerosol and gas content until the mid of this century they performed simulations applying different estimates for emissions in 2050. They scaled the 2016 emission fluxes in regard to the IPCC RCP scenarios. The detailed description of this approach and the results are presented in chapter 4.

In the 5th chapter of this deliverable, results with the global coupled aerosol climate model ECHAM6-HAM2 are presented. The simulations were performed and analysed by a research group from the Institute for Atmosphere and Climate at the Eidgenössische Technische Hochschule Zürich (ETHZ). These global simulations have a coarse resolution of 200 km x 200 km. But the presented simulations consider the change in anthropogenic and natural emissions as well as future changes in climate and land cover. The aerosol module is online coupled to the atmospheric model. It accounts for direct and indirect aerosol effects. In the simulations the time period between 1996-2014, referred to as present day, and 2040-2060, referred to as future (2050), are covered. The simulations are based on the IPCC RCP4.5 and RCP8.5 scenarios. They investigate the change in aerosol concentrations

and the resulting impact on air quality and aerosol radiative forcing. An additional simulation with future emissions in today's climate is discussed.

Although simulations are done with very different models and approaches, they are complementary. The KIT performed a high-resolution impact study of aerosols on radiative forcing for 2 days in July 2016. The UPMC compared emission fluxes for summer in 2016 and 2050 with each other in their regional simulation. Also, the University of York discuss emission scenarios for 2016 and 2050 in regional as well in global simulations. The ETHZ performed global scenarios for present day and mid of the century with a coupled aerosol climate model.

2 KIT

2.1 Model description

The simulations are performed with the coupled aerosol atmosphere model COSMO-ART (Baldauf et al., 2011; Vogel et al., 2009). The model and the simulation setup are further described in table 2.1.

Table 2.1: Model system summary and simulation setup

Characteristics	Description
Model version	COSMO5.1-ART3.1 (Baldauf et al., 2011; Vogel et al., 2009)
Time period	2-3 July 2016
Simulation domain	9.0°W–4.4°E, 3.0°N–10.8°N
Grid mesh size	2.5 km (0.0223°)
Vertical levels	80 up to 30 km (28 in the lowest 1.5 km ASL)
Meteorological boundary and initial data	COSMO-ART (5 km grid mesh size using ICON operational forecasts from DWD)
Pollutant boundary and initial data	COSMO-ART (5 km grid mesh size using MOZART, 2017) GlobCover (2009) landuse data CCSM (2015) plant functional types
Cloud microphysics	Two-moment microphysics scheme (Seifert and Beheng, 2006)
Pollutant emissions	Mineral dust (online): Rieger et al. (2017) using HWSD (2012) Sea salt (online): Lundgren et al. (2013) DMS (online): using Lana et al. (2011) BVOCs (online): Weimer et al. (2017) Biomass burning (prescribed/online): Walter et al. (2016) using GFAS (CAMS, 2017) Anthropogenic (prescribed): EDGAR (2010) Gas flaring (prescribed): Deetz and Vogel (2017)

Aerosol dynamics	MADEsoot (Riemer et al., 2003; Vogel et al., 2009)
	Secondary inorganic aerosol: ISORROPIA II (Fountoukis and Nenes, 2007)
	Secondary organic aerosol: VBS (Athanasopoulou et al., 2013)
Chemical mechanisms	Gas phase chemistry: RADMKA (Vogel et al., 2009)
Aerosol direct effect (ADE)	Vogel et al. (2009)
Aerosol indirect effect (AIE)	Warm phase: Bangert (2012) and Fountoukis and Nenes (2005)
	Cold phase: Philipps et al. (2008)

2.2 Aerosol sensitivity study assessing the effect of anthropogenic aerosol increase on atmospheric dynamics over SWA

In a process study, we focused on the aerosol impact on clouds and the atmospheric dynamics over SWA using the regional-scale model framework COSMO-ART (Vogel et al., 2009) for the simulation period 2-3 July 2016. The model setup is described in Table 1. Instead of using emission scenarios, two factors F_{ADE} and F_{AIE} were introduced in COSMO-ART, which allows defining different atmospheric burdens of aerosol by scaling the total aerosol mass and number densities, respectively. Table 2.2 summarizes the realizations used in this study, which are denoted as clean (0.25), reference (1.0) and polluted (4.0). Since the meteorological conditions show less variation from day to day, it is assumed that, even with a focus on a very short time period, insight can be achieved that can be generalized at least qualitatively to the length of the Post-onset phase (22 June – 20 July; Knippertz et al., 2017).

Table 2.2: Overview of the COSMO-ART realizations capturing the variation in the aerosol amount with respect to the Aerosol Direct Effect (ADE) and Aerosol Indirect Effect (AIE).

Abbreviation	Description of Simulation
$AIE_{0.25}ADE_{0.25}$	$F_{AIE}=0.25$ and $F_{ADE}=0.25$ (clean case)
$AIE_{1.0}ADE_{1.0}$	$F_{AIE}=1.0$ and $F_{ADE}=1.0$ (reference case)
$AIE_{4.0}ADE_{4.0}$	$F_{AIE}=4.0$ and $F_{ADE}=4.0$ (polluted case)

The simulations denoted in Table 2.2 (capturing the red rectangle in Fig. 2.1) are the result of a nesting into a 5 km COSMO-ART simulation (blue rectangle in Fig. 2.1a) using the ICON operational forecasts as meteorological boundary conditions.
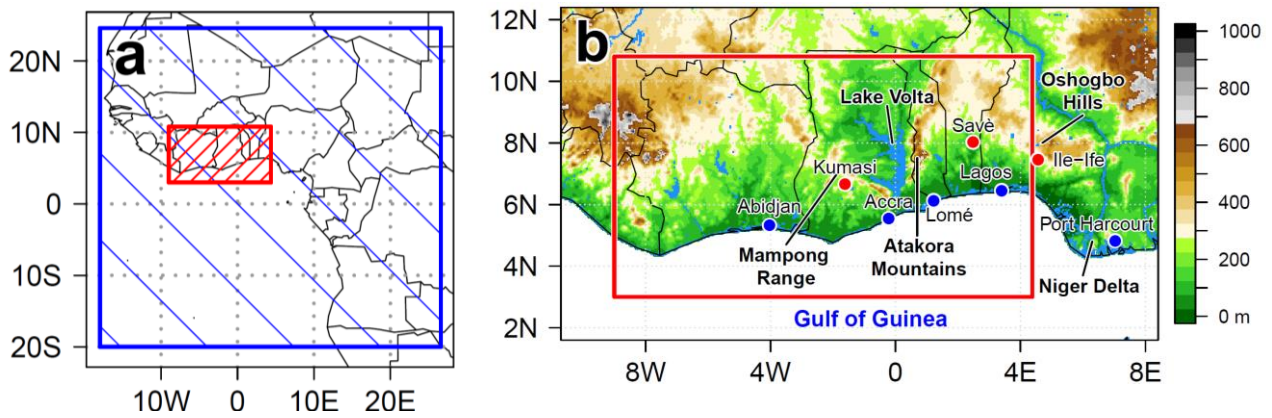
Figure 2.1: (a) Modeling domain SWA (red rectangle, 2.5 km grid mesh size) together with its coarse domain (blue, 5 km grid mesh size). (b) Map of the research area SWA. The color shading denotes the topography (m above sea level, ASL). Topographic features are named in bold, coastal cities are shown as blue dots and the three DACCIWA supersites as red dots. The modeling domain SWA is again denoted as red rectangle.

Figure 2.2 is a schema we depict to emphasize the general meteorological patterns relevant for the subsequent process study. In the nighttime a frequent occurrence of a nocturnal low-level jet (NLLJ, black arrows in Fig. 2.2a) can be observed with a jet maximum at 300 m above ground level (AGL) of around 6 m s^{-1} (Kalthoff et al., 2017). The nocturnal low level stratus (NLLS) is formed at the height of the jet maximum via shear-driven vertical mixing of moisture and maintained via cloud-top radiative cooling (Schuster et al., 2013). Also topographic lifting (Schuster et al., 2013; Adler et al., 2017) as well as vertical cold air advection in gravity waves and cloud formation upstream of existing clouds contribute to the NLLS formation (Adler et al., 2017). After sunrise a gradual Stratus-to-Cumulus Transition (SCT) takes place (e.g. Kalthoff et al., 2017). This is accompanied by a lifting of the cloud base (Fig. 2.2b). The increase of the liquid water path shortly after sunrise might be related to the growth of the convective boundary layer. Further analysis of this topic will be conducted within the framework of DACCIWA using observational data gathered during the ground-based field campaign. In the morning hours the maximum spatial coverage of NLLS can be observed (Fig. 2.2b). In the subsequent hours the NLLS deck breaks up to cumuliform clouds (Fig. 2.2c). Adler et al. (2017) identify a regular occurrence of a stationary coast-parallel front over SWA about 30 km inland that propagates inland during undisturbed monsoon conditions after about 16 UTC. Similar characteristics were described in Grams et al. (2010) for Mauritania. They indicate that the stationarity results from a balance between horizontal advection with the monsoon flow over the ocean and inland turbulence in the boundary layer that mixes the momentum vertically (Fig. 2.2d). With the reduction in turbulence in the afternoon the front begins propagating inland. The studies of Grams et al. (2010) and Adler et al. (2017), both based on modeling studies using COSMO, highlight the need to distinguish this feature from the land-sea breeze and the sea breeze front, since the dominating monsoon flow suppress the formation of a land wind during night. In the following, we use the term Atlantic Inflow (AI) as proposed by Grams et al. (2010), which is connected with an AI front and an AI airmass located behind the front.
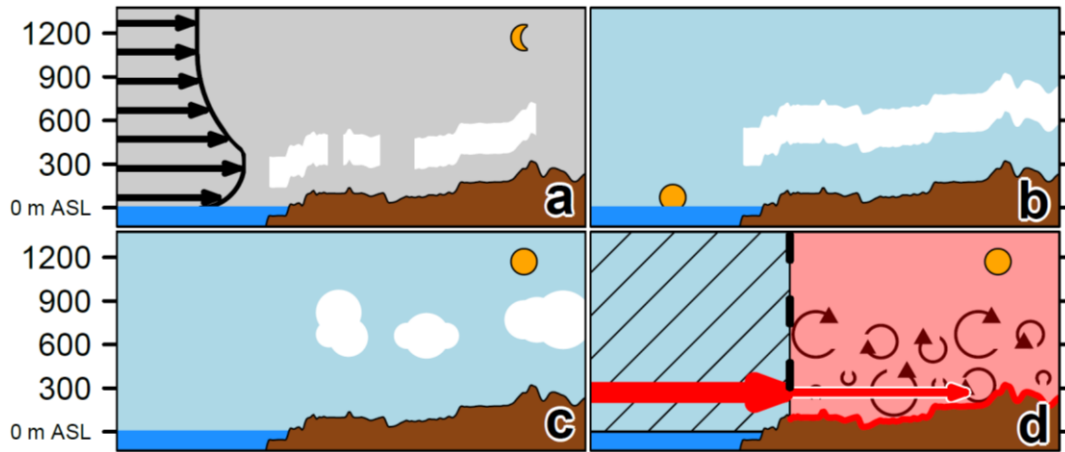
Figure 2.2: Schematic view on SWA atmospheric dynamics via a meridional-vertical transect (m ASL) through the Gulf of Guinea (blue shading) and adjacent land (brown shading). (a) During nighttime the NLLJ leads to a wind maximum at about 300 m AGL as emphasized by the black arrows. Over land, NLLS forms in the level of the NLLJ axis. (b) The maximum spatial coverage of NLLS is reached in the morning hours. After sunrise a lifting of the cloud base height can be observed. (c) During late morning or early afternoon the NLLS deck breaks up to cumuliform clouds. (d) Furthermore, during daytime the momentum of the onshore monsoon flow (bold red arrow) is mixed vertically over land due to atmospheric turbulence from solar heating (eddies). The balance between the monsoon flow and the turbulence leads to a frontal structure inland from the coast (black dashed line).

All the realizations in Table 2.1 exhibit the AI phenomenon. Following Grams et al. (2010), the AI front position can be estimated by the location at which a specific isentrope of virtual potential temperature $\theta_{v,s}$ crosses a specific height h_s. For Mauritania Grams et al. (2010) used $\theta_{v,s}$=310 K at the surface pressure level. For this study, reasonable results are achieved by using the potential temperature θ_s=302 K and the height h_s=250 m AGL. These values are selected empirically and are related to the COSMO-ART results of this study.
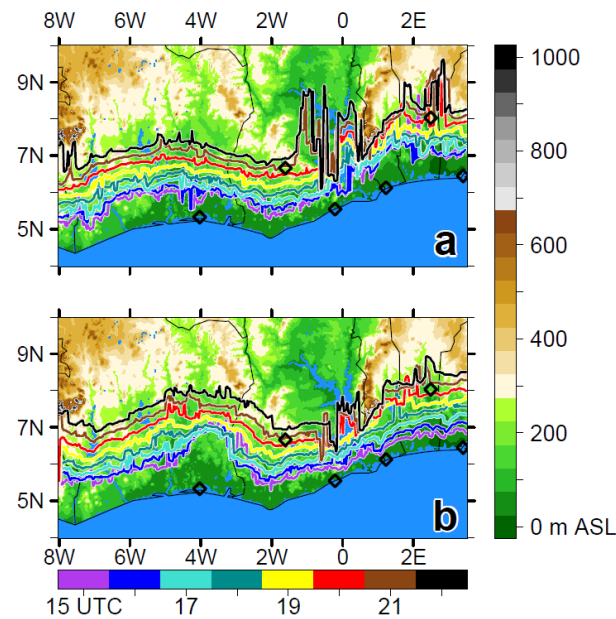

Figure 2.3: Localization of the AI front on (a) 2 July 2016 and (b) 3 July 2016 between 15 and 22 UTC for the reference case. The front is detected by the arrival of the isentropic surface θ_s=302 K at h_s=250 m AGL. The color of the front denotes the time (UTC, bottom legend). The underlying shading shows the topography of SWA (m, ASL, legend on the right). The black diamonds denote the cities shown in Figure 2.1.

Figure 2.3 shows the location of the AI front between 15 and 22 UTC for 2 July 2016 (Fig. 2.3a) and 3 July 2016 (Fig. 2.3b) in the reference case. Although the focus is on 2 July, 3 July is 15 UTC is added to underline that the AI is a robust feature occurring frequently over SWA, which is also indicated by the results of Adler et al. (2017). We focus on the front location of the time period 15–22 UTC, which shows an inland propagation of the AI front with time (coded by the line colors). Generally, the front is parallel to the coast. This is most obvious for the domain west of 2°W. In contrast, the Lake Volta area and also the area east of the Atakora Mountains show higher variability in the frontal location. Lake Volta is a flat area with fixed surface temperatures in the model and reduced roughness, likely affecting the frontal propagation. For the following analysis, the focus is set to Ivory Coast (7.5–3.0°W). The distance between the hourly frontal locations reveals that in the evening (approximately 15–18 UTC) the propagation velocity is small at the beginning but accelerates. At 15 UTC the front is located about 100 km inland. Before 15 UTC the AI front is not detectable, since the inland area is subject to warming, which shifts θ_s in coastal direction. However, between 11 UTC and 15 UTC already a horizontal wind speed gradient develops in an area between the coastline and 100 km inland with enhanced (reduced) values over the Gulf of Guinea (over land). The estimated frontal propagation velocity for the reference case on 2 July stagnates around 7 ms^{-1} after 19 UTC.

Figure 4 shows the meridional vertical transect of wind speed and potential temperature for the clean (Fig. 2.4a) and polluted case (Fig. 2.4b). When comparing the results between the clean and polluted case aerosol-specific characteristics can be identified. Whereas the temperature characteristics over the ocean are similar for the realizations, the inland temperature decreases with increasing aerosol amount. This is especially visible in the pre-frontal area but also the post-frontal area shows lower temperatures for the polluted case (Fig. 2.4b) than for the clean case (Fig. 2.4a). In the polluted case the advective cooling is more effective since the daytime inland near-surface air is a priori cooler due to a lower sensible heat flux from aerosol extinction. The reduced ocean-land temperature gradient in the polluted case leads to reduced temperature contrasts at the AI front (compare the 302 K isentrope for the clean case (bold line in Fig. 2.4a) and the polluted case (bold line in Fig. 2.4b)). With the change in the ocean-land temperature gradient, the AI frontal position and the NLLJ strength and vertical extension is altered. The higher the aerosol amount the more the AI front is lagging behind and the weaker the NLLJ. In the polluted case the vertical extension of the inland NLLJ and its wind speed in the jet axis is reduced by about 150 m and 2–3 m s^{-1}, respectively. The AI frontal difference averaged over Ivory Coast at 21 UTC is 10 km between the clean and reference case and 20 km between the clean and the polluted case. With the decrease in temperature with increasing aerosol amount, the pre-frontal wind speed generally increases (contrarily to the post-frontal area). This leads with respect to the polluted case (Fig. 2.4b) to some areas of increased wind speed in the pre-frontal area, at a height that is typical of the NLLJ. Generally, the polluted case is characterized by a blurring of the pre- and post-frontal temperature and wind speed differences.
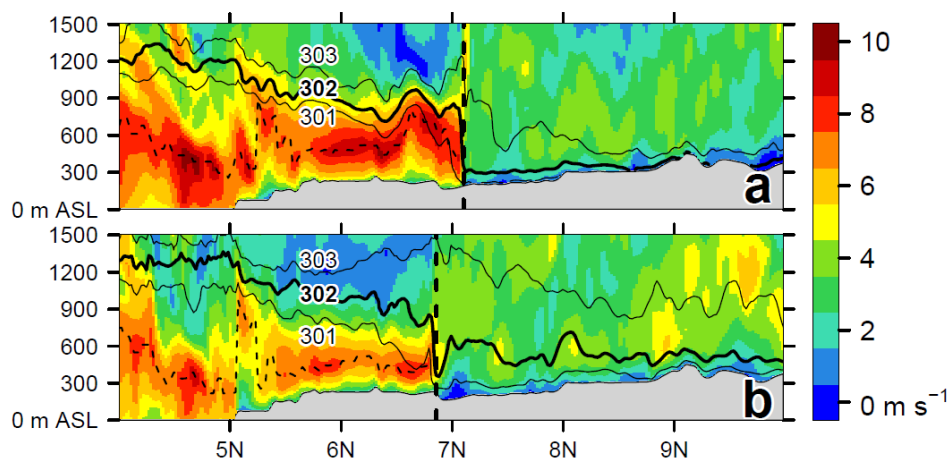

Figure 2.4: Meridional vertical transect (m ASL) of wind speed (shading, m s^{-1}) and potential temperature (isolines, K) along 5.75°W (central Ivory Coast) for 2 July 21 UTC with respect to (a) clean case and (b) polluted case. The bold isoline shows the 302 K isentrope that is used for the identification of the AI front (vertical dashed line). The horizontal dashed line shows the NLLJ wind speed maximum (jet axis) in the AI post-frontal area. The gray shading indicates the topography.

The two counteracting mechanisms turbulence and pressure gradient determine AI. With respect to the turbulence mechanism, a reduced heating weakens the turbulence in the PBL. Therefore, the AI balance between the monsoon flow and the inland turbulence is shifted to the monsoon flow, favoring an inland propagation. Regarding the pressure gradient, a reduced heating decreases the land-sea pressure gradient, shifting the AI balance to the opposite direction and suppressing the inland propagation. Therefore, two regimes can be observed: the first before 17 UTC and the second after 17 UTC. The first regime includes the stationary phase of the AI front near the coast. With the decrease in incoming solar radiation with increasing aerosol the turbulence decreases and therefore the stationary front location shifts inland. It is interesting that the location of the AI front during its stationary phase over Ivory Coast could be used as a proxy for the aerosol burden in that area (under otherwise identical conditions). For the time period after 17 UTC, when turbulence has decreased sufficiently, the pressure gradient mechanism dominates, because the AI front in the clean case - although lagging behind at 15 UTC, is 11 km ahead of the reference case at 22 UTC. Figure 5 summarizes the counteracting components turbulence and pressure difference that govern the inland propagation of the AI front by comparing the temporal evolution of the differences between the reference and clean case (dashed lines) and the polluted and reference case differences (solid lines) in surface sensible heat flux (red, positive downward) and surface pressure (blue), spatially averaged for the AI pre-frontal area over Ivory Coast. The temporal evolution clearly shows that the sensible heat flux differences (and the absolute values itself) decrease strongly with time in contrast to the pressure differences. After sunset (e.g. 18:24 UTC at Kumasi) the sensible heat flux is negligible but the pressure differences continue. In fact, the altered land-sea pressure gradient is maintained till the AI front and the subsequent cool airmass has passed the area and compensates the differences (not shown). It is expected that the high moisture in the monsoon layer prevents the layer to cool significantly and to reduce the differences that developed during daytime. The factor increase of 4 from 1.0 to 4.0 reduces (increases) the sensible heat flux (sea level pressure) more than the increase from 0.25 to 1.0. The differences between the realizations are finally equalized by the passage of the AI front and post-frontal airmass.
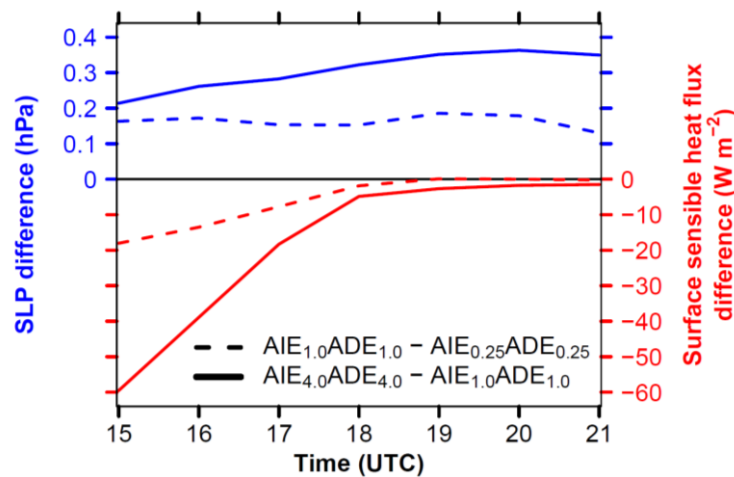

Figure 2.5: Temporal evolution of the differences in surface sensible heat flux (red, W m^{-2}) and surface pressure (blue, hPa) between the reference and the clean case (dashed line) and between the polluted and the reference case (solid line) for the time period 2 July 15-21 UTC spatially averaged for the AI pre-frontal area over Ivory Coast as defined by the θ_s method. The sensible heat flux is defined positive downward.

In addition to the aerosol impact on AI, also impacts on the SCT can be observed. Less shortwave radiation reaches the ground with increased amounts of aerosol and therefore also the surface sensible heat fluxes decrease. To underline that this effect is visible for the entire SWA region, Figure 2.6 shows the temporal evolution of the spatial average of total cloud cover (Fig. 2.6a), total cloud water (Fig. 2.6b) and the cloud base height (Fig. 2.6c) over SWA, for the clean (blue dashed), reference (black solid) and polluted case (red solid). Between 21 UTC and the time of sunrise (5:30 UTC) the cloud cover increases (Fig. 2.6a) due to clouds that are advected onshore or develop inland. This is linked with a reduction in the mean cloud base (Fig. 2.6c). Between 1 UTC and 7 UTC

the clean case shows lower cloud base values than the reference and polluted case. A detailed analysis reveals that this deviation is not related to NLLS but to mid-level clouds over the Lake Volta Basin and in the northwestern part of the domain (not shown). After sunrise it is assumed that the NLLS intensifies via vertical mixture of moisture in the developing convective PBL. With respect to the spatial average in Figure 2.6c this leads to a reduction in mean cloud base height. The maximum cloud cover (Fig. 2.6a) is related to the minimum cloud base (Fig. 2.6c), underlining the dominance of NLLS. After reaching the cloud cover maximum, the SCT continues, which is related to a lifting of the cloud base and a decrease in cloud cover. For this SCT a clear temporal shift of about one hour can be observed between the clean and the reference case and two hours between the clean and the polluted case. The realizations with increased aerosol amounts react slower to the insolation after sunrise, reach the NLLS maximum coverage later and start later with the SCT. After 15 UTC this finally leads to a cloud cover that is increased compared to the clean case (Fig. 2.6a) implying an additional reduction in surface shortwave radiation that can be used for further cooling the surface and decelerating the AI front. The cloud water (Fig. 2.6b) shows a similar temporal shift with increasing aerosol amounts as for the cloud cover and cloud base. The weakening of the SCT with a higher aerosol burden leads to reduced amounts of cloud water after 13 UTC (Fig. 2.6b) likely due to reduced convective activity. However, during nighttime, the polluted case uniformly shows higher cloud water values than the clean and reference case.
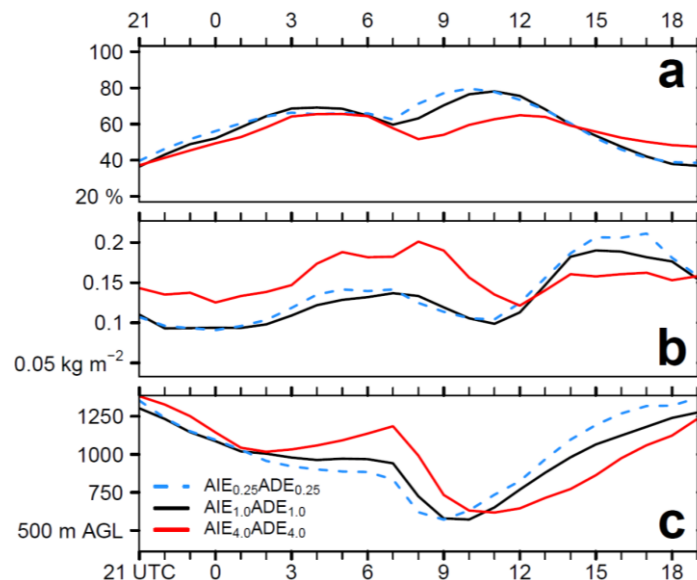

Figure 2.6: Spatial average (8°W-3.5°E, 5-10°N) of (a) total cloud cover (%), (b) total cloud water (kg m^{-2}) and (c) cloud base height (m AGL) for the temporal evolution between 2 July 21 UTC and 3 July 19 UTC. The cloud cover is detected by non-zero values of the total cloud water. A value of 60 % denotes that 60 % of the domain is covered by clouds. For the spatial average of total cloud water, values below 10 g m^{-2} were omitted. The cloud base height is detected via the lowest height AGL with a non-zero cloud water value. The blue dashed, black solid and red solid lines denote the clean, reference and polluted case, respectively.

2.3 Conclusions

We showed that AI affects the entire SWA domain through the course of the day via cold air advection, the NLLJ that can be found in the AI post-frontal area and convergence-induced convection and precipitation. Two distinct meteorological responses to changes in the amount of aerosol via ADE and the Twomey effect were identified: *1. A spatial shift of the Atlantic Inflow (AI) and 2. A temporal shift of the Stratus-to-Cumulus Transition (SCT).*
Figure 2.7 shows a conceptual model that combines both responses. The bigger loop is related to the first response (AI) and the smaller loop to the second (SCT). Following the AI loop in Figure 2.7, the increase in the amount of aerosol (number and mass) by a factor of 4 (0.25 to 1.0) is the initial perturbation of the system. The subsequent numbers in parenthesis are related to the median value over Ivory Coast (cloud-free inland areas) on 2 July 15 UTC to provide guiding values for the denoted changes.

Via ADE the aerosol increase leads to a decrease in surface net downward shortwave radiation (-37 W m^{-2}) and surface temperature (-0.5 K). Previous studies showed that till the early afternoon, the AI front is stationary near the coast due to the balance between the monsoon flow from the sea and the sensible heat flux (turbulence) over land. With the afternoon decrease in sensible heat flux, the AI front propagates inland. This study showed that the decreased surface heating leads to a positive pressure anomaly over land (+0.16 hPa) and with that to a reduced land-sea pressure gradient. The latter is more persistent than the sensible heat flux that vanishes around sunset (compare Fig. 2.5). The reduced pressure gradient leads to a reduced AI frontal velocity and therefore to a southward shift in the case of increased aerosol (11 km on 2 July 22 UTC). The post frontal area is characterized by stronger wind speeds in the lowest 1000 m AGL with the maximum around 250 m AGL that is characteristic of the NLLJ. Therefore, an AI frontal shift leads to a shift in the NLLJ inland propagation. Since the AI frontal propagation is linked to convergence-induced convection and convective precipitation, also a meridional shift of the AI-related precipitation is observed. These effects are primarily related to the afternoon but the AI frontal and NLLJ shift also leads to a shift in the inland propagation of coastal NLLS with a similar spatial magnitude as observed for the AI front (not shown). The AI loop denoted in Figure 2.7 includes a further mechanism, related to the counteracting effects of the monsoon flow over the ocean and the sensible heat flux over land in the stationary phase of the AI front. With increasing aerosol, the inland sensible heat flux decreases, which relocates the front farther from the coast. Therefore, with increased aerosol the AI frontal inland propagation starts farther from the coast but is slower than in the low aerosol case due to the reduced land-sea pressure gradient as soon as the turbulence has declined after sunset.
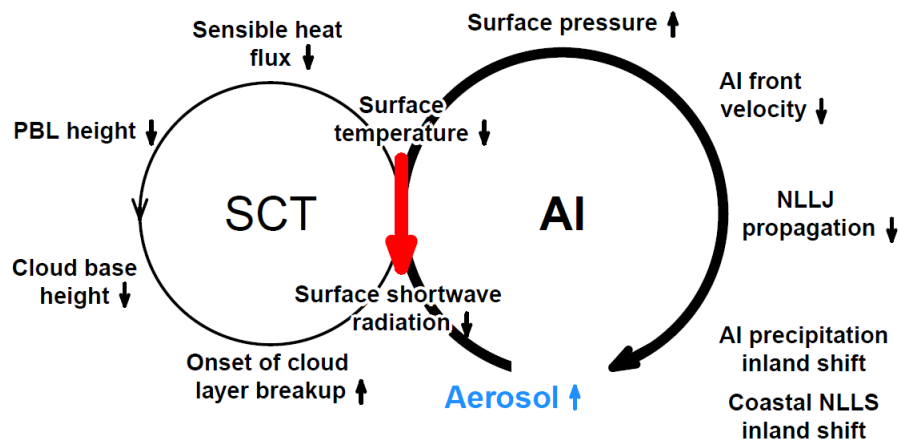

Figure 2.7: Scheme of the aerosol-related atmospheric feedbacks summarizing the findings of the process study simulations on 2-3 July 2016. The main loop is labeled AI (Atlantic Inflow) and the additional loop SCT (Stratus-to-Cumulus Transition). The small arrows in upward and downward direction denote whether a quantity reacts with a decrease (downward) or increase (upward) to the increase of aerosol mass and number (blue) as the initial perturbation. The red arrow shows the linkage between AI and SCT via the decrease in shortwave radiation and surface temperature and a potential pathway for a negative feedback of SCT on AI.

The SCT loop is coupled to the AI loop via the decrease in surface shortwave radiation and temperature. This study pointed out that the deficit in surface heating due to ADE and cloud brightening via the Twomey effect lead to a decrease in sensible heat flux and therefore to a delayed development of the CBL. The lower CBL height leads to a lower cloud base and therefore to a later SCT and breakup of the closed cloud layer to scattered cumuli. Both loops are initialized after sunrise with the input in shortwave radiation. The SCT loop reveals a positive cloud cover anomaly after 15 UTC with increasing aerosol. The sunset is around 18:30 UTC. Although the AI front already starts penetrating inland around 14-15 UTC, approximately a 3.5-hour period is available for an additional surface cooling from the later cloud-layer breakup. This is a pathway for a further deficit in surface shortwave radiation and surface heating that could further weaken the AI loop as emphasized by the red arrow in opposite direction in Figure 2.7. However, the latter coupling between the two loops is only hypothesized. A future study needs to assess the significance of the contribution in inland

surface pressure increase that comes from the deficit in shortwave heating via the later cloud-layer breakup. The mechanisms described in Figure 2.7 raise the question about the possibility to generalize these results. The AI feature is very likely a regular phenomenon under undisturbed monsoon conditions as confirmed by previous studies that focus on longer time periods. Within this process study the AI frontal shift was obvious for both days in the evening. However, the results presented above are related to Ivory Coast that shows a more coherent AI frontal pattern than the eastern part of the domain, likely related to topographic features. This conceptual picture reveals radiation as a key player governing the feedbacks, either via ADE or via a change in cloud albedo (Twomey effect). The AIE assessment within the process study reveals the known mechanisms, in particular the increase (decrease) of the CDNC (effective radius) with an increase in the aerosol number concentration. However, the AI-related clouds and precipitation reveal, aside from a meridional shift, no statistically significant difference. Although, the possibility for substantial effects from AIE cannot be excluded, a conceptual view as presented for the radiative effects has to be left for subsequent studies.

A future study could address the AI frontal displacement detection in long-term observations. A potential strategy is the analysis of the AI front around noon via remote sensing cloud observations from past to present by assuming a positive trend in the aerosol burden. It is expected that the daytime AI front location has shifted landwards from the past to current conditions but also other phenomena (e.g. decadal SST variations) have the potential to affect the front location.

3 UPMC

In order to quantify the impact of the future anthropogenic emissions, two simulations are done using the WRF and CHIMERE models. The meteorology and the boundary conditions are the same and represents the period from 1st June to 30th September 2016. The modelled region corresponds to a large domain centred on the Gulf of Guinea and with a constant horizontal resolution of 60kmx60km. The WRF-CHIMERE is used in its off-line configuration. The model set-up is presented in Table 3.1.

CHIMERE is a chemistry-transport model allowing the simulation of concentrations fields of gaseous and aerosols species at a regional scale. In this study, the version fully described in Menut et al. (2013a) and updated in Mailler et al. (2016) is used. If the simulation is performed with the same horizontal domain, the 28 vertical levels of the WRF simulations are projected onto 20 levels from the surface up to 200 hPa for CHIMERE. The chemical evolution of gaseous species is calculated using the MELCHIOR2 scheme. The photolysis rates are explicitly calculated using the FastJX radiation module (version 7.0b, Wild (2000); Bian (2002)). The modelled AOD is calculated by FastJX for the several wavelengths over the whole atmospheric column. At the boundaries of the domain, the climatology from global model simulations are used. In this study, outputs from LMDz-INCA (Hauglustaine et al., 2014) are used for all gaseous and aerosols species, except for mineral dust where the simulations from the GOCART model are used (Ginoux et al., 2001).

Table 3.1: WRF-CHIMERE model set-up.

Model name	Spatial extent	Gas phase Chemistry	Anthropogenic emission	Mineral aerosols emission	Sea salt aerosols emission	Biogenic components emission	Vegetation fires emission
CHIMERE	Regional	Melchior reduced scheme	HTAP 2010 RCP8.5	Online (Alfaro and Gomes 2001)	Online (Monahan 1986)	Online (MEGAN)	Offline (CAMS)

The anthropogenic emissions are issued from the HTAP global database (Janssens et al., 2015) for the current period 2016 and from the IPCC RCP8.5 scenario for 2050. Due to the late in the DACCIWA emissions inventory (both for present and future), we turned to these inventories even if we know this is probably not the best product to make fine comparisons.

For a month of July, the NO2 surface emissions fluxes are presented in Figure 3.1. In the north of the Gulf of Guinea, the emissions have similar magnitude, but the spatial extent of the future emissions is larger than the present ones. Over the sea, the ship routes are also close in magnitude and follow the same trajectories. The main differences between the two emissions inventories is the number of urbanized areas with more cities in the future inventory.
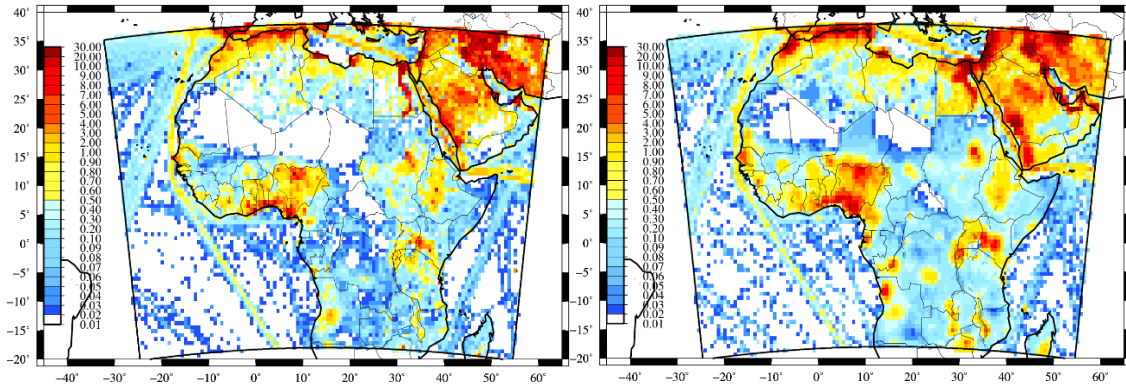

Figure 3.1: Monthly NO2 emission fluxes in tons/km2/month for July 2016 (left) and 2050 (right).

The vegetation fires emissions are quantified using the CAMS model of ECMWF. These fluxes correspond to daily averaged values, constantly distributed in each hours of the day. Vertically, the surface fluxes are injected in the low troposphere and homogeneously in the boundary layer. The mineral dust emissions are calculated using the Alfaro and Gomes (2001) scheme, optimized following Menut et al. (2005b) and using the soil and surface databases presented in Menut et al. (2013b).

The results are presented as time series of daily averaged differences between the two simulations, with anthropogenic emissions of 2016 and 2050. All other model parameters remain identical. The time series are for some sites, representative of various locations in the domain. These locations are represented in Figure 3.2.
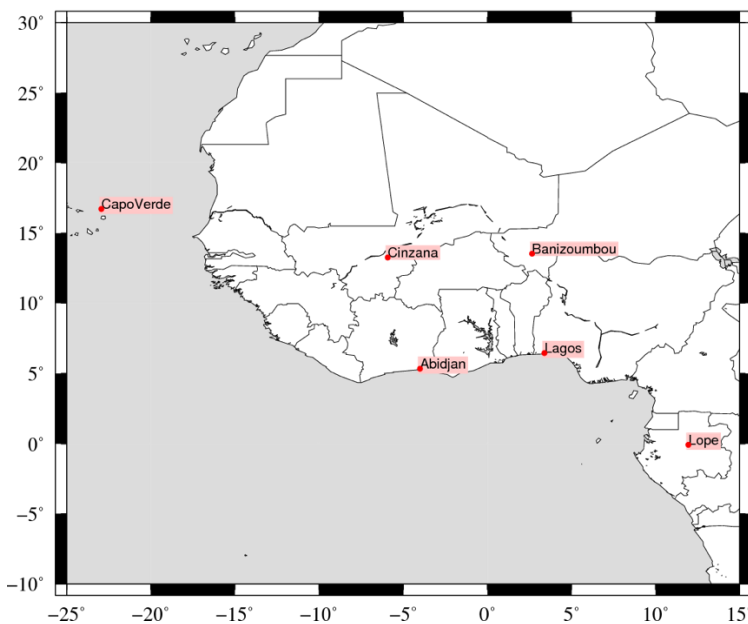

Figure 3.2: AERONET stations used in the report.

These locations were selected because:

- Lope represents a site close to the biomass burning emissions in Central Africa
- Abidjan and Lagos represent large urbanized areas in the Gulf of Guinea, where anthropogenic emissions are important and may evolve a lot in the future.
- Cinzana and Banizoumbou represent locations in the Sahelian area and are representative of major mineral dust sources
- Capo Verde represents a location under the plumes of mineral dust and anthropogenic pollution after long range transport.
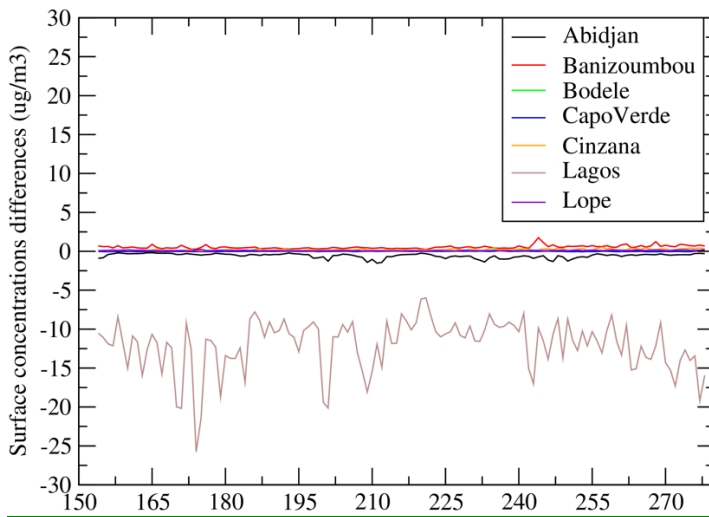

Figure 3.3: Difference in daily averaged NO$_2$ surface concentration at different stations between 2050 and 2016. The x-Axis is given in day of the year.

For NO$_2$ surface concentrations, the difference is low and between -2 and +2 µg/m^3, except for the site of Lagos where values are between -10 and -25 µg/m^3 (figure 3.3). It means that the future emissions are lower for this area and directly and locally impact the surface concentrations in this city. The differences are also negative in Abidjan, the other urbanized area, but in a lesser extent with values between 0 and -2 µg/m^3. For all other sites, the differences are positive, showing that the emissions are more important or more spatially concentrated. The important differences in Lagos may be due to a planned decrease of emissions in the future or to the way to spatially distribute the emissions. The two emissions inventories having different origins, it is difficult to conclude on this difference, only recorded in Lagos.
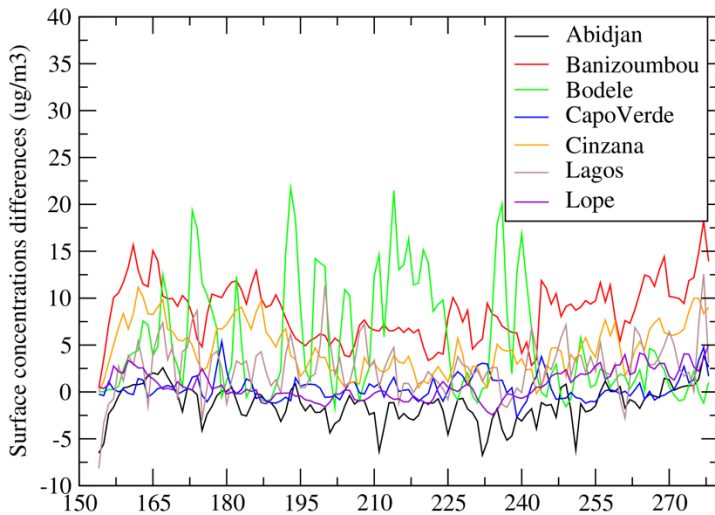
Figure 3.4: As figure 3.3, but for O₃.

For O$_3$ surface concentrations, the differences located in Abidjan and Lagos are low. The future emissions create lower O$_3$ concentrations (~-2 to -5 µg/m^3) in Abidjan and higher (0 to 5 µg/m^3) in Lagos (figure 3.4). For Lagos, this increase in O$_3$ seems low when comparing with the high decrease calculated in NO$_2$: the lower NO$_2$ flux in 2050 has not a large titration effect. For remote areas, such as Bodele, Cinzana, and Banizoumbou, the ozone concentration increases a lot in the future, with values higher by +10 to +20 µg/m^3.
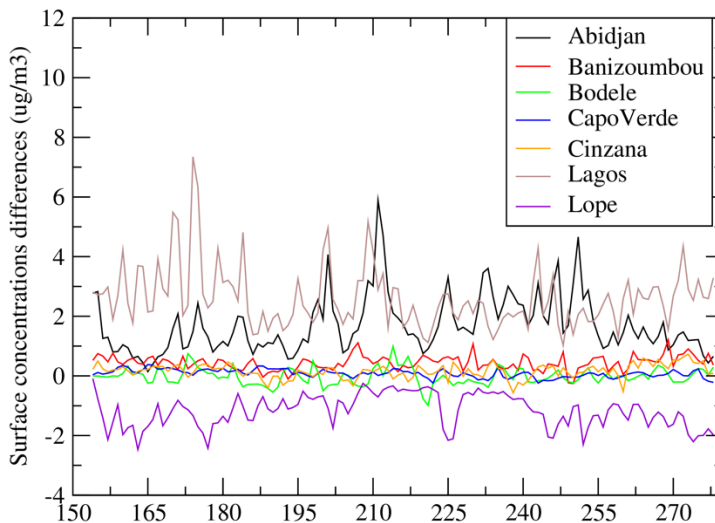

Figure 3.5: As figure 3.3, but for PM2.5.

In this region, a large part of PM2.5 is due to mineral dust and biomass burning. In this study, only anthropogenic emissions are changed and thus the differences are low and reflect only this contribution. Three different behaviours are modelled: (i) very low differences are modelled in Banizoumbou, Bodele, Capo Verde and Cinzana: far from the anthropogenic sources, the two simulations remain close. (ii) high positive differences are modelled in the large cities, Abidjan and Lagos, showing an increase in the future for Particulate Matter emissions. (iii) a decrease in Lope, mainly due to the scenarios of landuse and urbanization management in this area (figure 3.5).
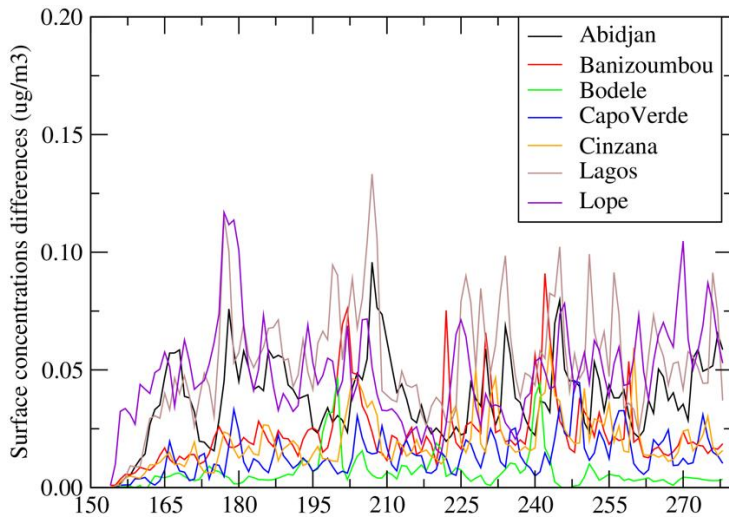
Figure 3.6: As figure 3.3, but for AOD.

The Aerosol Optical depth (AOD) is representative of the number of aerosols in the atmosphere. The differences are close to zero for the sites close to the mineral dust sources and far from the urbanized areas. Larger positive differences are modelled for the sites of Abidjan and Lagos as well as Lope, with values ranging between 0 and 0.15. The differences in AOD are positive for all sites (figure 3.6) when we noted a negative difference in PM2.5 in Lope. It is difficult to explain apart the fact that the size distribution, then the speciation of the emitted species is very different for this site and between the two emissions inventories.

Another way to quantify the impact of these two emissions inventories is to make maps of differences of surface concentrations or AOD. Examples of maps of differences are presented for NO_2, O_3 and AOD and for the 1st July 2016, 12:00 UTC.
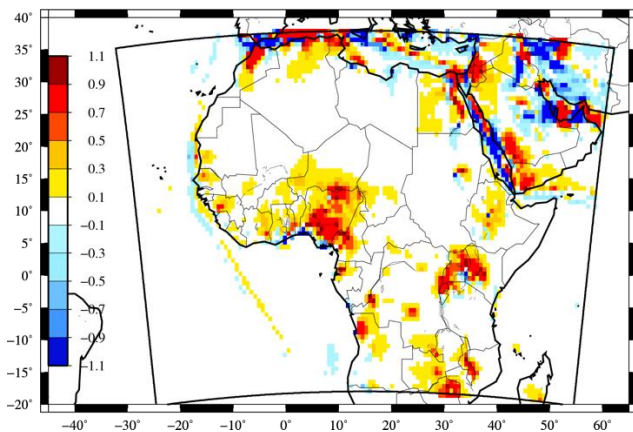

Figure 3.7: Difference in NO_2 surface concentration between 1st July 2050 and 2016.

The map for NO_2 shows three different things: (i) in the Gulf of Guinea and Central Africa, the future emissions are higher than for 2016 (figure 3.7). Some negative values are visible close to the coast but it may be only due to the difference of horizontal resolution of the two datasets. (ii) differences are negative or positive along the ships tracks. Here again, this is more probably due to a problem with the raw horizontal resolution of the inventories than to a realistic decrease or increase of the emissions flux over the ocean. (iii) In central Africa and at the north of the Gulf of Guinea, the NO_2 concentrations are clearly larger in 2015 than in 2016. For these areas, there is no doubt that anthropogenic emission fluxes are larger and have a non-negligible impact of surface concentrations.
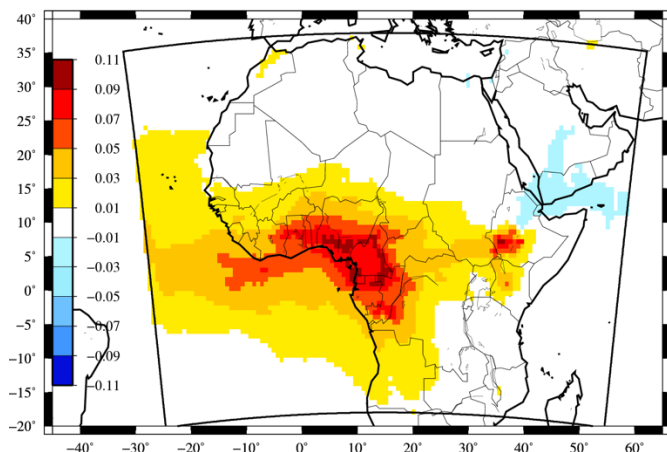
Figure 3.8: As figure 3.7, but for AOD.

The differences in AOD are more spatially homogeneous (figure 3.8). For the largest part of the studied domain, the future AOD is more intense than the present one. The values of differences are not very important and have a maximum of 0.1. A small area over Saudi Arabia has negative values but close to zero and probably linked to a spatial shift in emissions and then of AOD plumes.
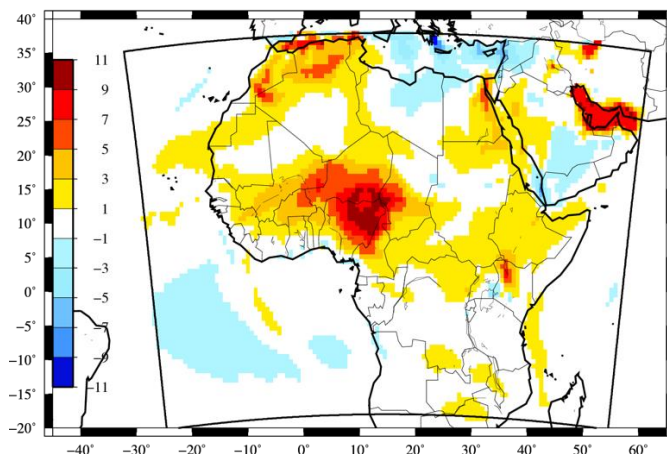

Figure 3.9: As figure 3.7, but for O_3.

For ozone, the differences are also mainly positive, showing an increase in future surface concentrations and between 0 and 10 µg/m^3 (figure 3.9). The increase in the future is mainly inland and in Africa. This large positive plume is representative of the changing emissions in the large urbanized areas of the Gulf of Guinea and represents the transport of ozone precursors from the coast to the north-east.

3.1 Conclusions

Two simulations were done with the WRF-CHIMERE models in off-line configurations. The only change between the two configurations are the anthropogenic emission fluxes, in order to extract only this contribution on the modelled chemical concentrations. By comparing the results with inventories for 2016 and 2050, it appears that an increase in surface concentrations of NO_2, O_3 and PM2.5 is estimated. The values are moderate and mainly above or at the north of the large urbanized areas along the coast of the Gulf of Guinea. One has to notice that some results have to be interpreted with care: the emission inventories being not built with the same methodology; some localized differences may be only due to different specializations and horizontal resolution of the raw emissions fluxes.

4 UoY

4.1 Model Overview

GEOS-Chem is a global and regional offline chemistry transport model (*www.geos-chem.org; Bey et al., 2001*). In this work, we have used a regional grid run at 0.25° x 0.3125° horizontal resolution over West Africa with one-way nested boundary conditions from a global 4° x 5° simulation (Figure 4.1). We have used GEOS-Chem v11-01 which contains a O_x, HO_x, NO_x, VOC, BrO_x chemistry scheme and a mass based aerosol module which advects SO_4^{2-}, NO_3^-, NH_4^+, Sea Salt, Dust, Organic and Black Carbon aerosol.

For 2016, our simulations use anthropogenic emissions from the DACCIWA inventory (*Junker et al., 2008*). However, based on the DACCIWA observations we scale these anthropogenic emissions for the West Africa region to better reflect the concentrations observed (see Deliverable 3.4). The emissions of NO from the DACCIWA inventory are scaled by a factor of 1.4 and the SO_2 emission by a factor of 10. Biogenic emissions use the MEGAN inventory (*Guenther et al., 2012*). Biomass burning uses GFAS emissions from ECMWF (*Kaiser et al., 2009*) with a scale factor of 3.4 on OC emissions as suggested by *Kaiser et al.* (*2012*). Dust follows the work of *Zender et al.* (*2003 a,b*), sea salt of *Alexander et al.* (*2005*) and *Jaeglé et al.* (*2011*), marine emissions of DMS are from *Breider et al.* (*2017*), biogenic soil NO_x emissions from *Hudman et al.* (*2012*) and lightning NO_x is described by *Murray et al.* (*2012*).

In this study, simulations have been run for the year 2016 and the year 2050. The future simulations for 2050 have been based upon the IPCC RCP scenarios, further detail of the emissions used for these simulations is given in Section 4.2. Changes in the concentrations of pollutants in West Africa due to the changes in photo-pollutants have been investigated for the period of the DACCIWA aircraft campaign (29th June – 16th July).
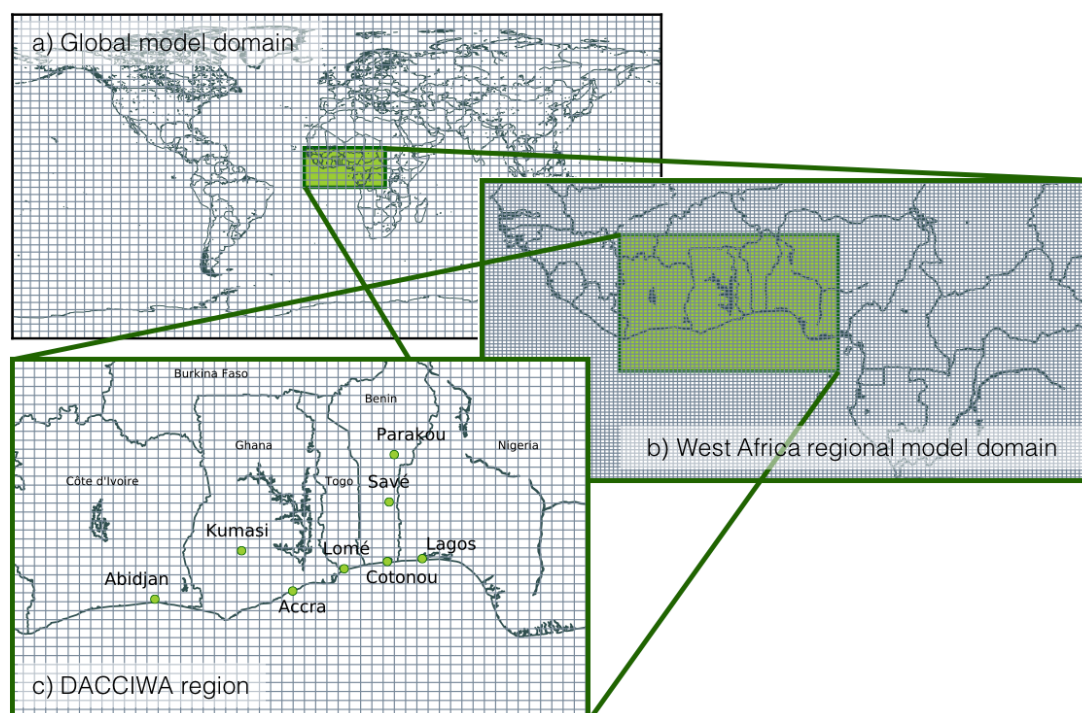

Figure 4.1: Global and regional GEOS-Chem grids used in the modelling work described here. a) shows the global domain; b) shows the regional domain run at 0.25° x 0.3125° covering West Africa from the Atlantic coast to central Africa; c) shows the DACCIWA operational area with the grid spacing used.

4.2 Future emission inventories for West Africa

In this study, simulations have been run the years 2016 and 2050. The simulation for 2016 uses anthropogenic emissions from the DACCIWA inventory (*Junker et al., 2008*) with the corrections described earlier based on the observational data collected during the DACCIWA field campaign. For 2050 we use the same emissions and meteorology for all but the anthropogenic inventory. We scale the 2016 emissions (corrected DACCIWA emissions) by the ratio of the emissions predicted by the Intergovernmental Panel on Climate Change (IPCC) Representative Concentration Pathway (RCP) scenarios between 2016 and 2050. We do this to provide the best possible simulation of the present day, with the 2050 scenarios taking this increase into account. Thus, a set of future emission inventories for Africa have been created for each of the four RCP scenarios which are summarised in Table 4.1.

The RCP emissions data is provided at 10 year intervals. The ratio between the 2050 and 2010 RCP emissions has been determined spatially for the whole African continent and this ratio data has been used to scale the 2010 DACCIWA anthropogenic emissions, whilst incorporating the emission scaling determined for 2016, to create an anthropogenic emission inventory for the year 2050. The RCP emission data contains a breakdown of emissions by source – agricultural sector, agricultural waste burning, residential and commercial combustion, energy production and distribution, industrial processes and combustion, solvent production and use, land transport and waste treatment and disposal. Each of the sources have been considered separately in the construction of the 2050 inventory data and the present day DACCIWA emissions have been scaled by the ratios from the corresponding sources.

Table 4.1: Summary of IPCC RCP scenarios.

RCP Scenario	Summary	References
RCP 2.6	A so-called "peak" scenario with the radiative forcing level reaching a value around 3.1 W m^{-2} mid century, returning to 2.6 W m^{-2} by 2100.	*van Vuuren et al. (2007)*
RCP 4.5	A stabilisation scenario where total radiative forcing is stabilised to 4.5 W m^{-2} by 2100 by employing a range of technologies and strategies for reducing greenhouse gas emissions.	*Smith et al. (2006)* *Clarke et al. (2007)* *Wise et al. (2009)*
RCP 6.0	A stabilisation scenario where total radiative forcing is stabilised to 6 W m^{-2} by 2100 employing a range of technologies and strategies for reducing greenhouse gas emissions.	*Fujino et al. (2006)* *Hijioka et al. (2008)*
RCP 8.5	A scenario of increasing greenhouse gas emissions over time leading to high greenhouse gas concentration levels.	*Riahi et al. (2007)*

Figures 4.2 – 4.5 show the 2016 and 2050 emissions of carbon monoxide (CO), nitrogen oxides (NO$_x$), sulfur dioxide (SO$_2$), organic carbon aerosol (OC), black carbon aerosol (BC) and non-methane volatile organic compounds (NMVOCs) for the West Africa region for each of the RCP scenarios. They also show the ratio between the future and present day emissions to illustrate how each species is projected to change under each scenario.

Figure 4.2: RCP 2.6 emissions of CO, NO$_x$, SO$_2$, OC, BC and NMVOCs for West Africa from the DACCIWA anthropogenic emission inventory. The first panel shows the emissions used in the 2016 simulation whilst the second panel shows the emissions for 2050 which are scaled based upon RCP 2.6. The third panel shows the ratio between the 2050 and 2016 emissions - green indicates a decrease in emissions and red indicates an increase in emissions between 2016 and 2050.
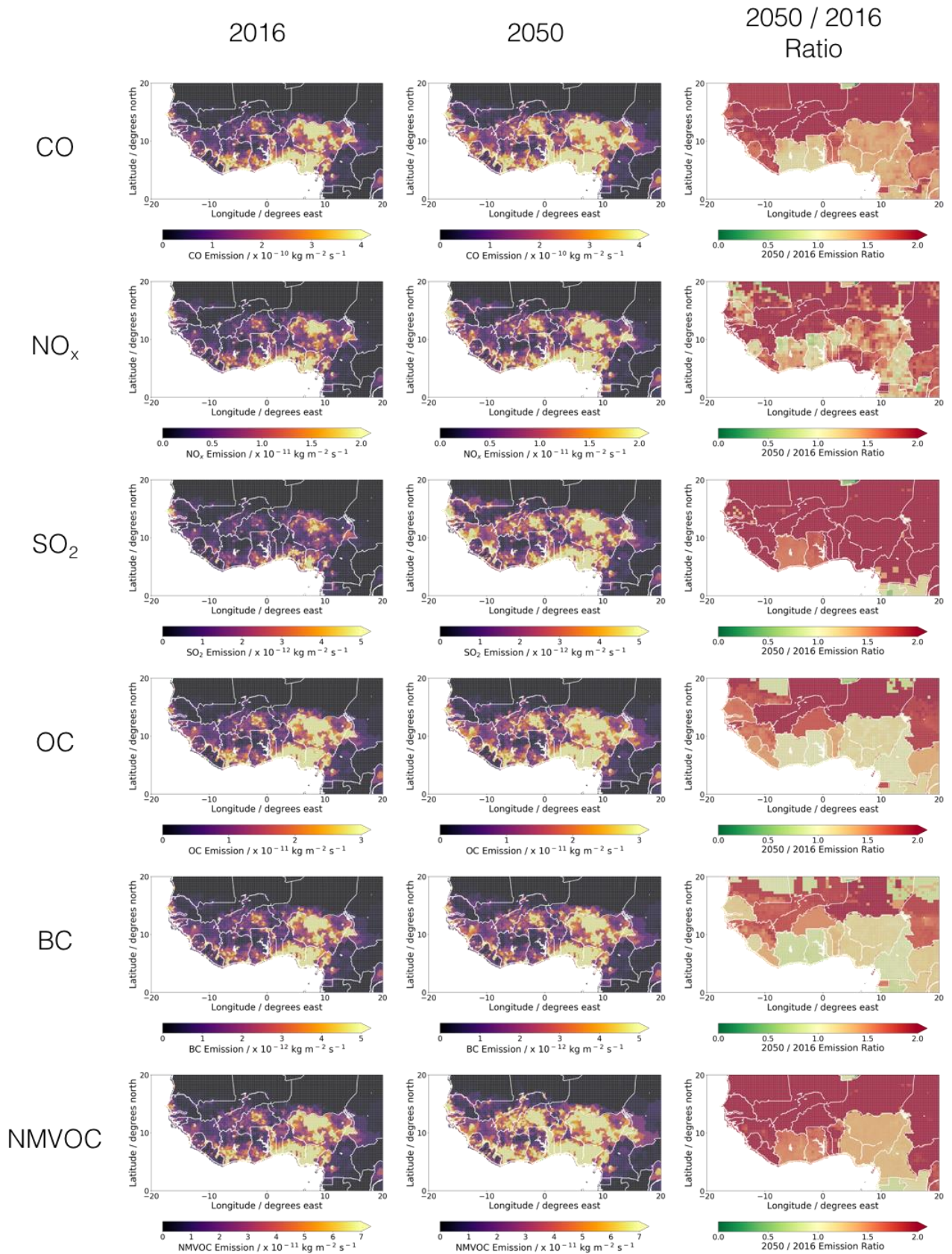
Figure 4.3: RCP 4.5 emissions of CO, NO_x, SO_2, OC, BC and NMVOCs for West Africa from the DACCIWA anthropogenic emission inventory. The first panel shows the emissions used in the 2016 simulation whilst the second panel shows the emissions for 2050 which are scaled based upon RCP 4.5. The third panel shows the ratio between the 2050 and 2016 emissions - green indicates a decrease in emissions and red indicates an increase in emissions between 2016 and 2050.
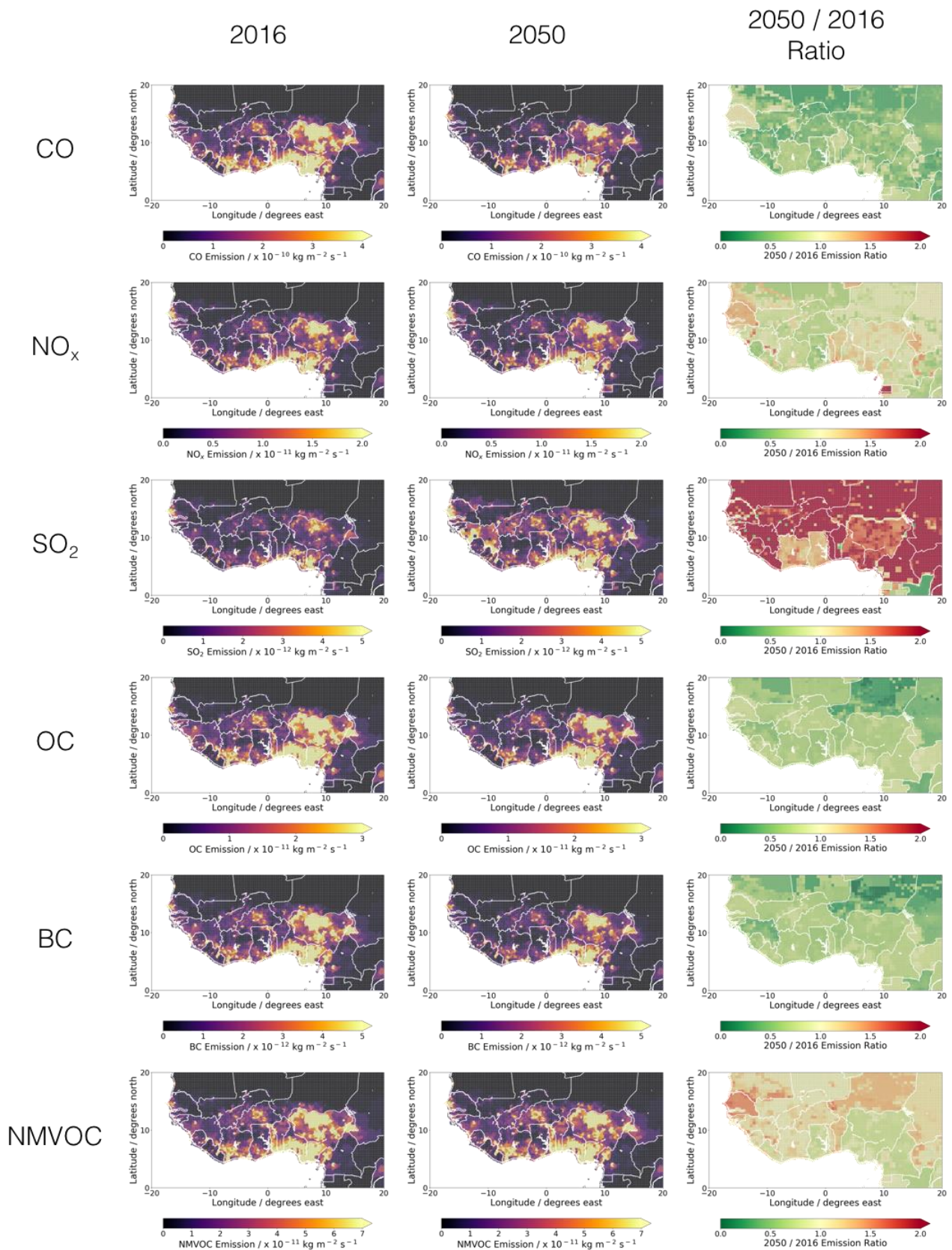
Figure 4: RCP 6.0 emissions of CO, NO$_x$, SO$_2$, OC, BC and NMVOCs for West Africa from the DACCIWA anthropogenic emission inventory. The first panel shows the emissions used in the 2016 simulation whilst the second panel shows the emissions for 2050 which are scaled based upon RCP 6.0. The third panel shows the ratio between the 2050 and 2016 emissions - green indicates a decrease in emissions and red indicates an increase in emissions between 2016 and 2050.
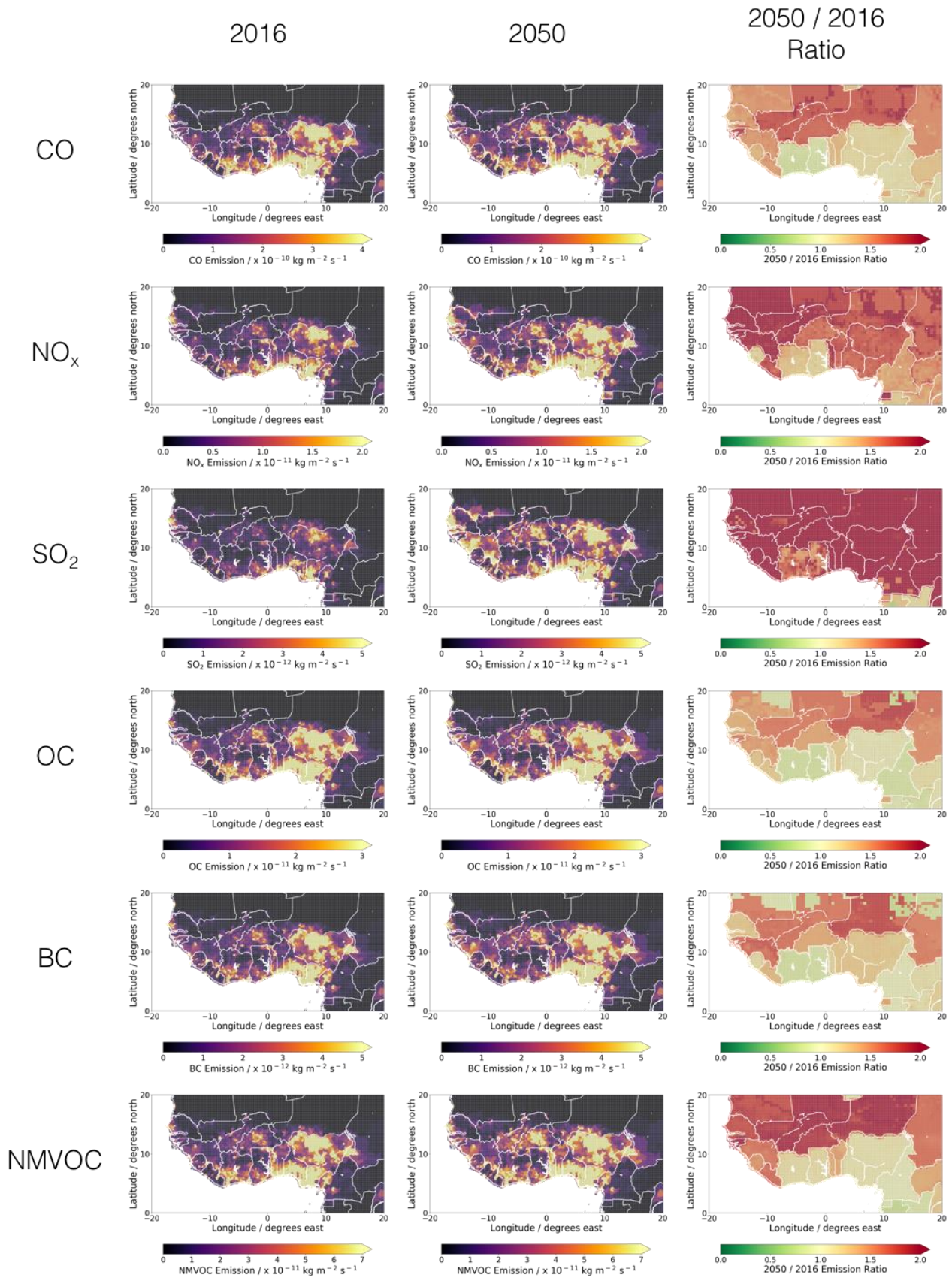
Figure 5: RCP 8.5 emissions of CO, NOx, SO2, OC, BC and NMVOCs for West Africa from the DACCIWA anthropogenic emission inventory. The first panel shows the emissions used in the 2016 simulation whilst the second panel shows the emissions for 2050 which are scaled based upon RCP 8.5. The third panel shows the ratio between the 2050 and 2016 emissions - green indicates a decrease in emissions and red indicates an increase in emissions between 2016 and 2050.
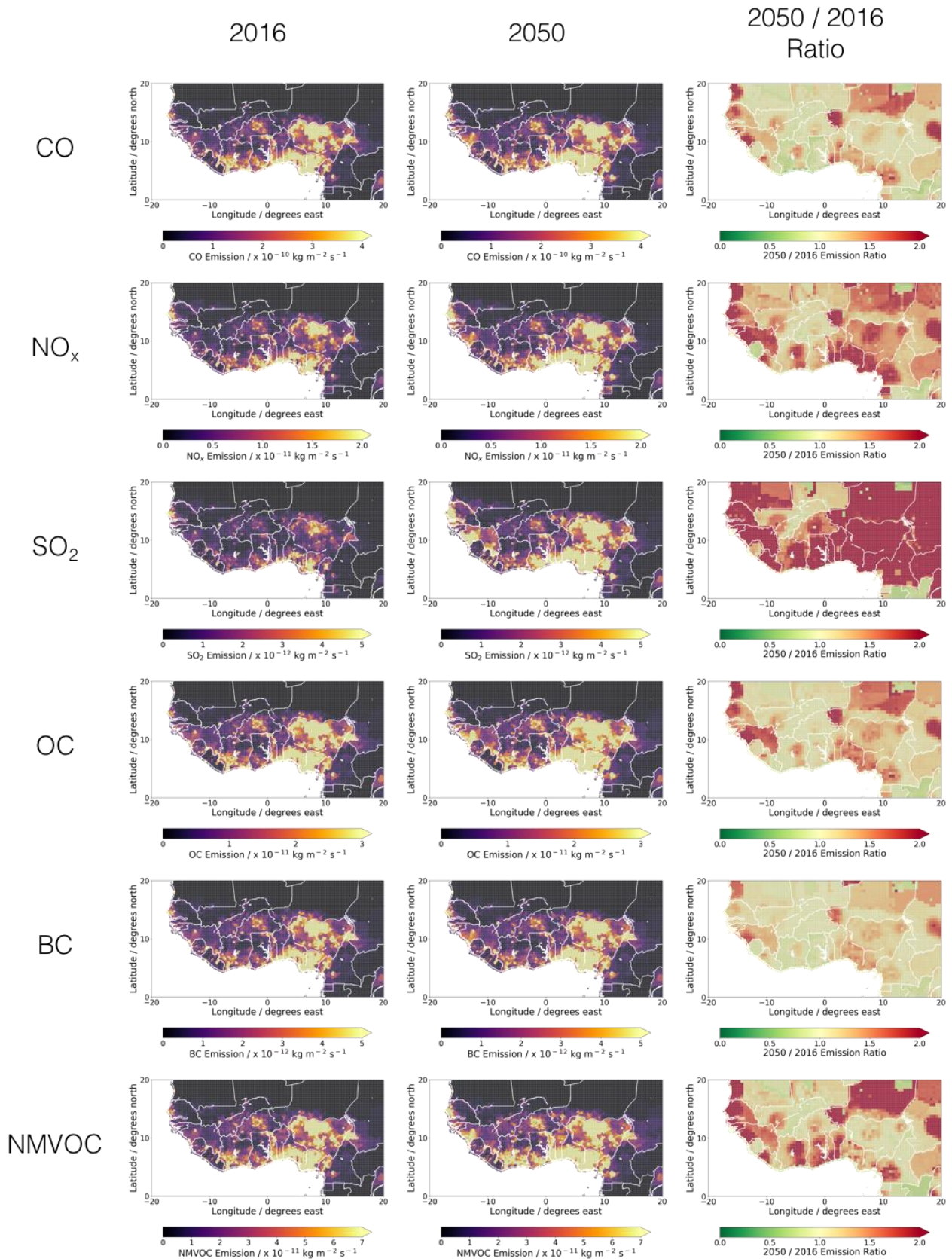
It is evident that there are substantial differences between the predictions made by the different RCP for the different pollutants in 2050. There is not a straight forwards relationship between the change in the pollutant and the RCP or the changes between the pollutants within one RCP. In general they all show increases in the emissions of air pollutants but, for example, RCP 6.0 typically shows reductions in the emissions of pollutants (other than SO_2). There is a complicated and relatively inconsistent vision of the future or air pollutants between the different RCPs. From an air quality perspective the range seen between the RCPs should be seen as a range of possible air quality futures which are potentially uncorrelated to the futures predicted by CO_2 or CH_4 emissions.

4.3 Simulations of present and future pollutant concentrations in West Africa

The model has been run, as described in Section 1, for 2016 and for 2050 using the four different emission scenarios described in Section 2. The simulations for 2050 use the same emissions (notably biomass burning), CH_4 concentrations, and meteorology as the 2016 simulation, with the only difference being in the anthropogenic emissions described in Section 2. The simulations have been performed using the West Africa nested model for the period of the DACCIWA aircraft campaign in 2016 and the equivalent period in 2050. Boundary conditions for the West Africa regional model have been generated from the global model at 4° x 5° resolution using the same set of emission inventories. The model output has been used to investigate how the concentrations of pollutants in the DACCIWA region vary under each future projection scenario. This study focuses on fine particulate matter ($PM_{2.5}$), ozone (O_3) and nitrogen dioxide (NO_2), which are the air quality pollutants which can be simulated by the model.

We have run the model from 29th June to 16th July to cover the period of the DACCIWA campaign. Potential changes during other time periods (notably the winter biomass burning / dust season) have not been investigated.

4.3.1 Spatial variations in pollutant concentration
Figures 4.6 – 4.8 show the spatial distribution of $PM_{2.5}$, O_3 and NO_2 in West Africa in 2016 and 2050 for each of the RCP scenarios.

Figure 4.6: Spatial variations in PM$_{2.5}$ concentration for West Africa under each RCP scenario. The first panel shows the 2016 mean concentration, the second panel shows the 2050 mean concentration, the third panel shows the absolute difference between 2016 and 2050, and the fourth panel shows the percentage change from 2016 to 2050. All data displayed in this figure is an average of hourly data at surface level from the DACCIWA aircraft campaign period (29th June – 16th July).
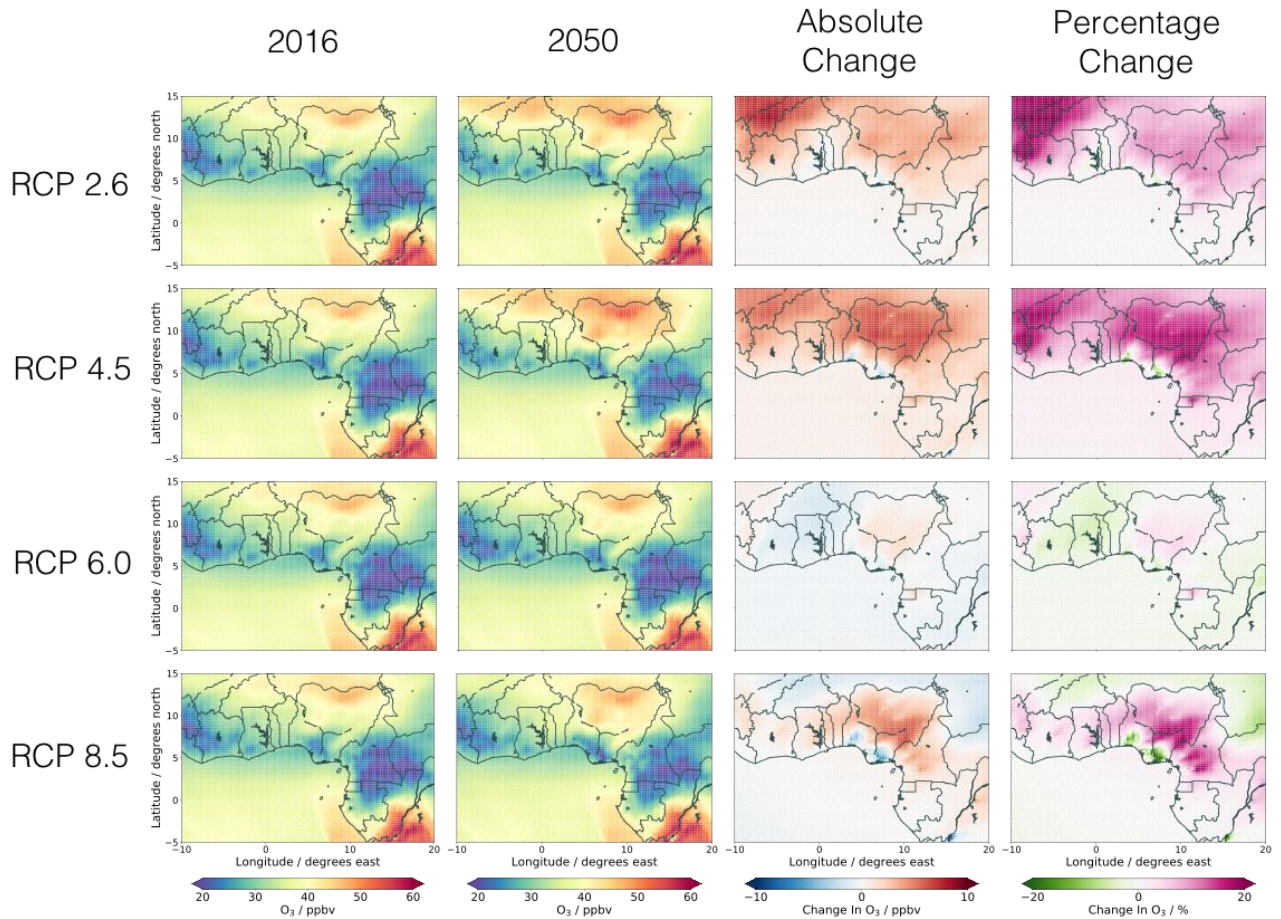
Figure 4.7: Spatial variations in O_3 concentration for West Africa under each RCP scenario. The first panel shows the 2016 mean concentration, the second panel shows the 2050 mean concentration, and the third panel shows the absolute difference between 2016 and 2050, and the fourth panel shows the percentage change from 2016 to 2050. All data displayed in this figure is an average of hourly data at surface level from the DACCIWA aircraft campaign period (29th June – 16th July).
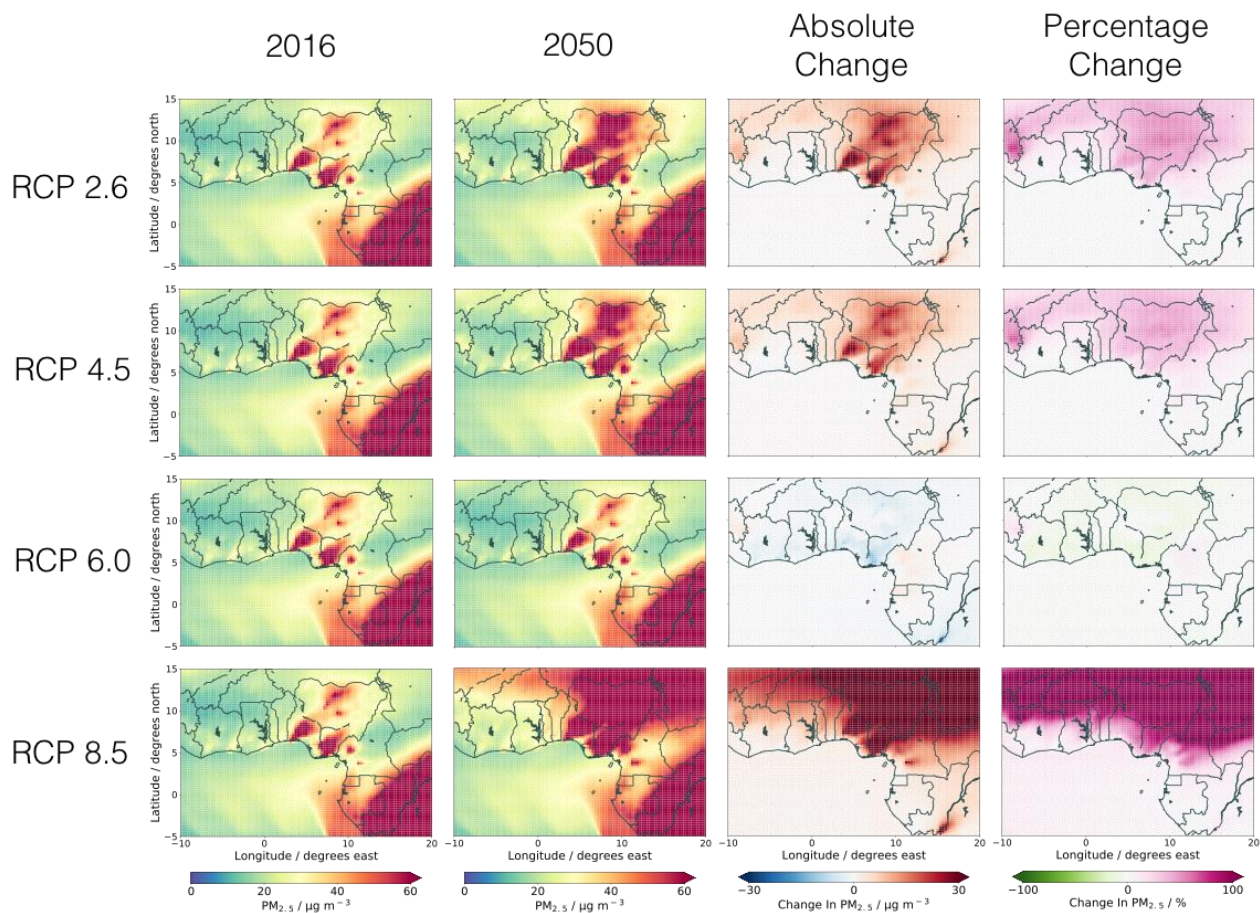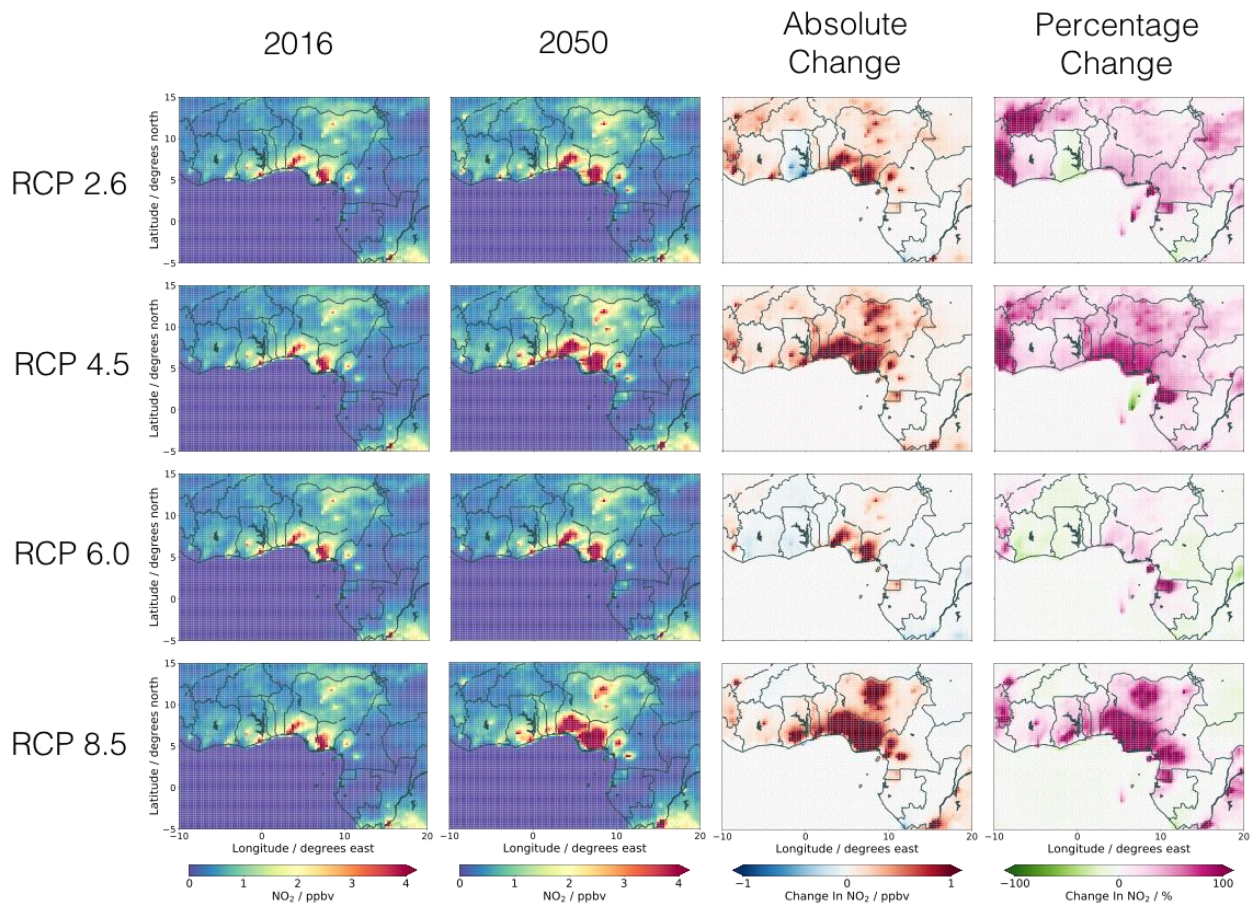
Figure 4.8: Spatial variations in NO₂ concentration for West Africa under each RCP scenario. The first panel shows the 2016 mean concentration, the second panel shows the 2050 mean concentration, the third panel shows the absolute difference between 2016 and 2050, and the fourth panel shows the percentage change from 2016 to 2050. All data displayed in this figure is an average of hourly data at surface level from the DACCIWA aircraft campaign period (29th June – 16th July).

Under the RCP 2.6, 4.5 and 8.5 scenarios the concentrations of the O_3, $PM_{2.5}$ and NO_2 increase. Under the RCP 6.0 scenario, the concentrations generally decrease moderately. Focussing on the RCP 8.5 scenario these increases are potentially very large with $PM_{2.5}$ concentrations doubling in Nigeria and increasing substantially in inland regions. Ozone concentrations increase marginally (10%) under RCP 8.5 but increase more for RCP 2.6 and 4.5. NO_2 concentrations double under most scenarios.

4.3.2   Temporal variation in pollutant concentration

The changes in surface level concentrations for six of the key coastal cities in West Africa have been examined. Figure 4.9 shows the locations of the cities being considered in this study.
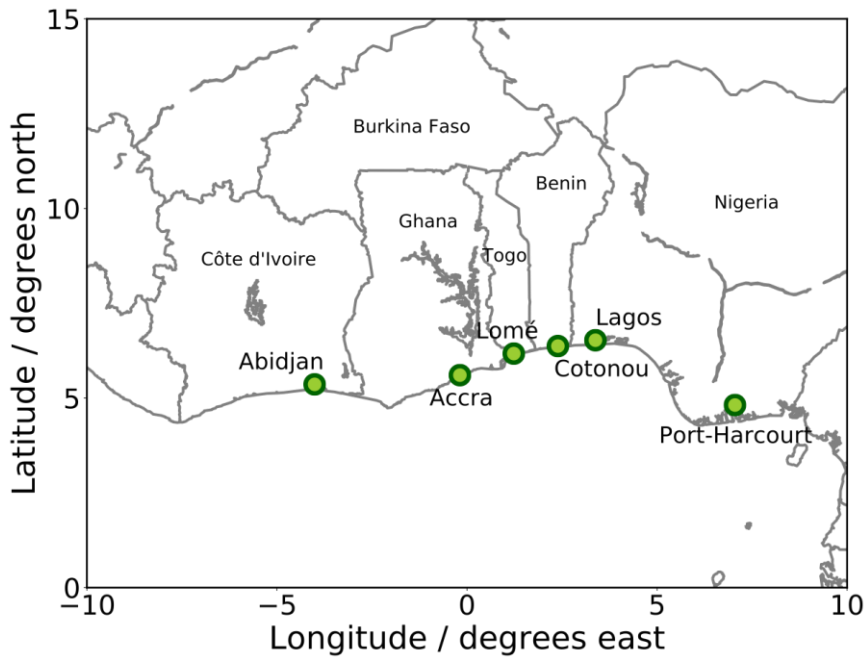
Figure 4.9: Location of some of the major coastal cities in the DACCIWA region: Abidjan, Côte d'Ivoire; Accra, Ghana; Lomé, Togo; Cotonou, Benin; Lagos, Nigeria; Port-Harcourt, Nigeria.

Figure 4.10 shows the changes in $PM_{2.5}$ concentration over the summer campaign period. These time series plots also indicate the WHO guideline limits for $PM_{2.5}$. In all cases, the annual mean limit of 10 µg m^{-3} is exceed, with the 24-hour mean limit of 25 µg m^{-3} also being exceeded on most occasions. It can be seen clearly that the $PM_{2.5}$ concentrations in the Nigerian cities of Lagos and Port-Harcourt are significantly higher than for other cities. However, the increases going toward 2050 for most of the DACCIWA cities are relatively minor.

Figure 4.10: Variations in PM_{2.5} concentrations over time for the DACCIWA aircraft campaign period for six of the West African coastal cities. This plot compares the model output for 2016 and for each RCP scenario for 2050. The coloured lines show the 6-hour mean concentrations from each of the simulations. The WHO annual mean limit (10 µg m⁻³) and 24-hour mean limit (25 µg m⁻³) guidelines are indicated by the black dashed lines.

Figure 4.11 shows the changes in O_3 concentration. The WHO guideline of 100 µg m^{-3}, equivalent to approximately 50 ppbv, is shown in the figure and in all cities the concentration of ozone remains below the guideline limit. There are some variations between the different scenarios but the concentration of O_3 generally remains unchanged between present day and 2050, averaging around 30 ppbv in each of the West African cities.

Figure 4.11: Variations in O_3 concentrations over time for the DACCIWA aircraft campaign period for six of the West African coastal cities. This plot compares the model output for 2016 and for each RCP scenario for 2050. The coloured lines show the 6-hour mean concentrations from each of the simulations. The WHO 8-hour mean limit (100 µg m^{-3}, equivalent to ~51 ppbv) guideline is indicated by the black dashed line.

Figure 4.12 shows the changes in NO_2 concentration over the campaign period. The WHO annual mean limit of 40 µg m^{-3}, equivalent to approximately 21 ppbv, is shown in the figure. In all cities, the average concentrations are below the WHO limit. These concentrations are also significantly lower than the WHO 1-hour mean limit of 200 µg m^{-3} (~ 106 ppbv).
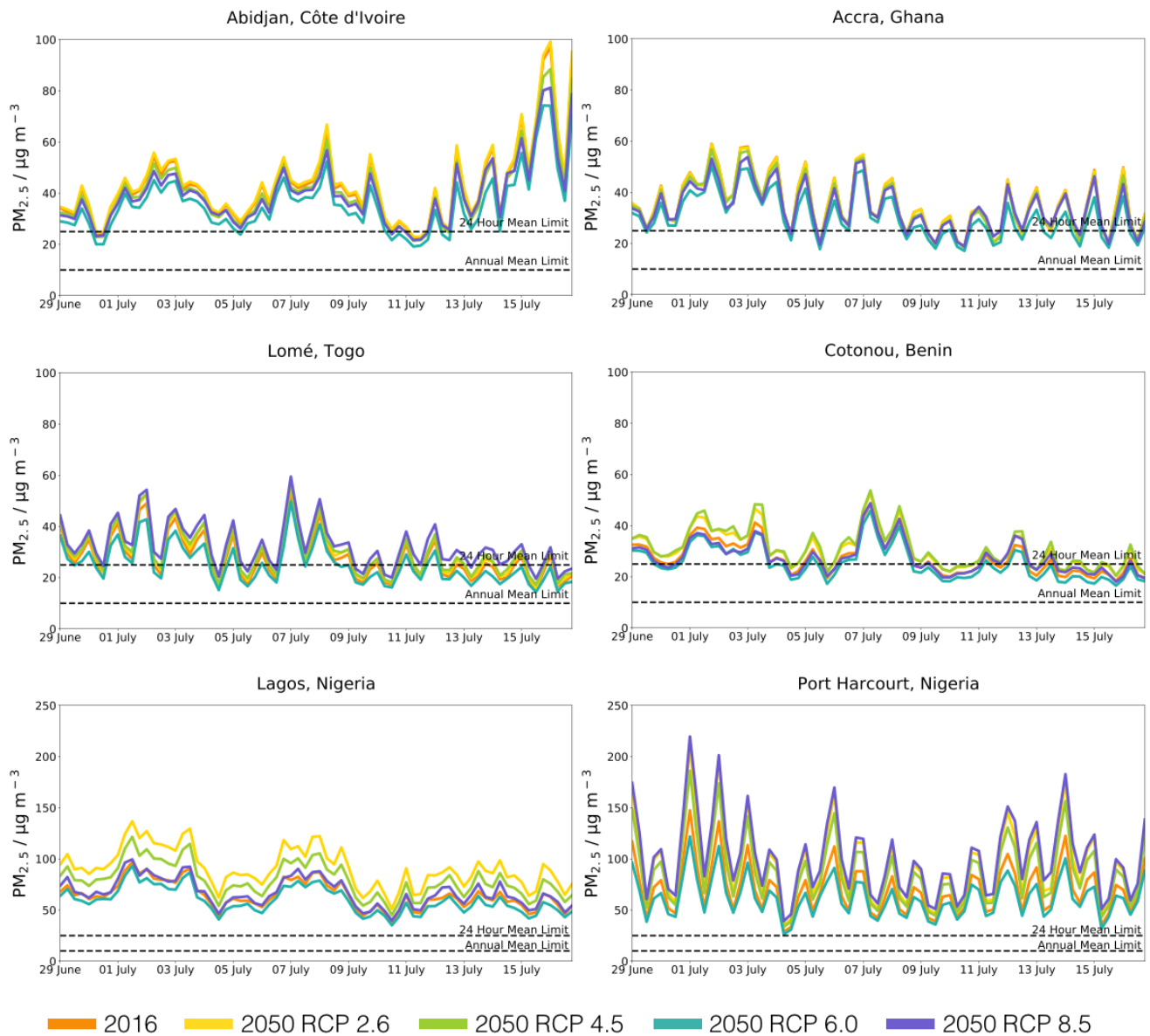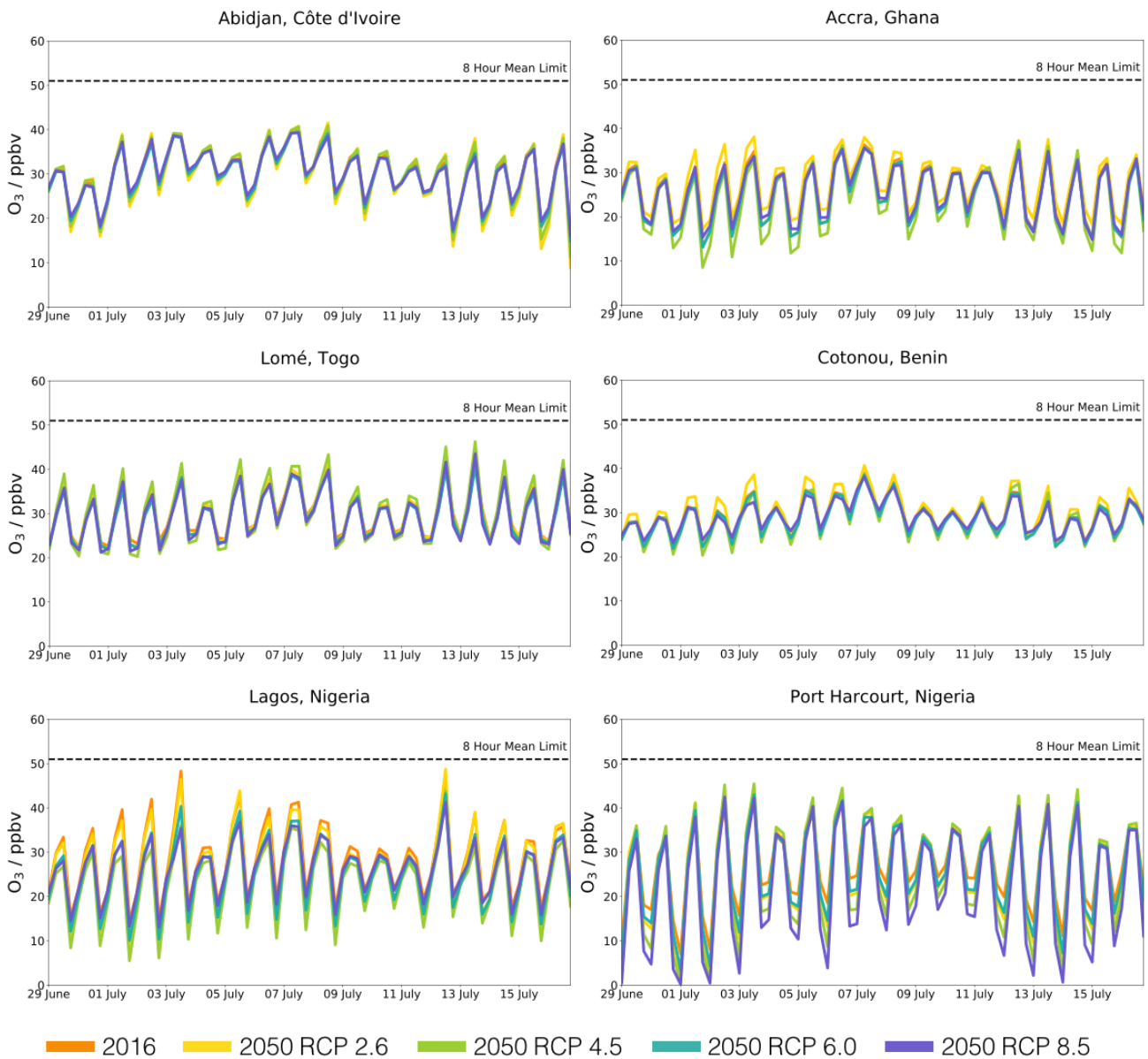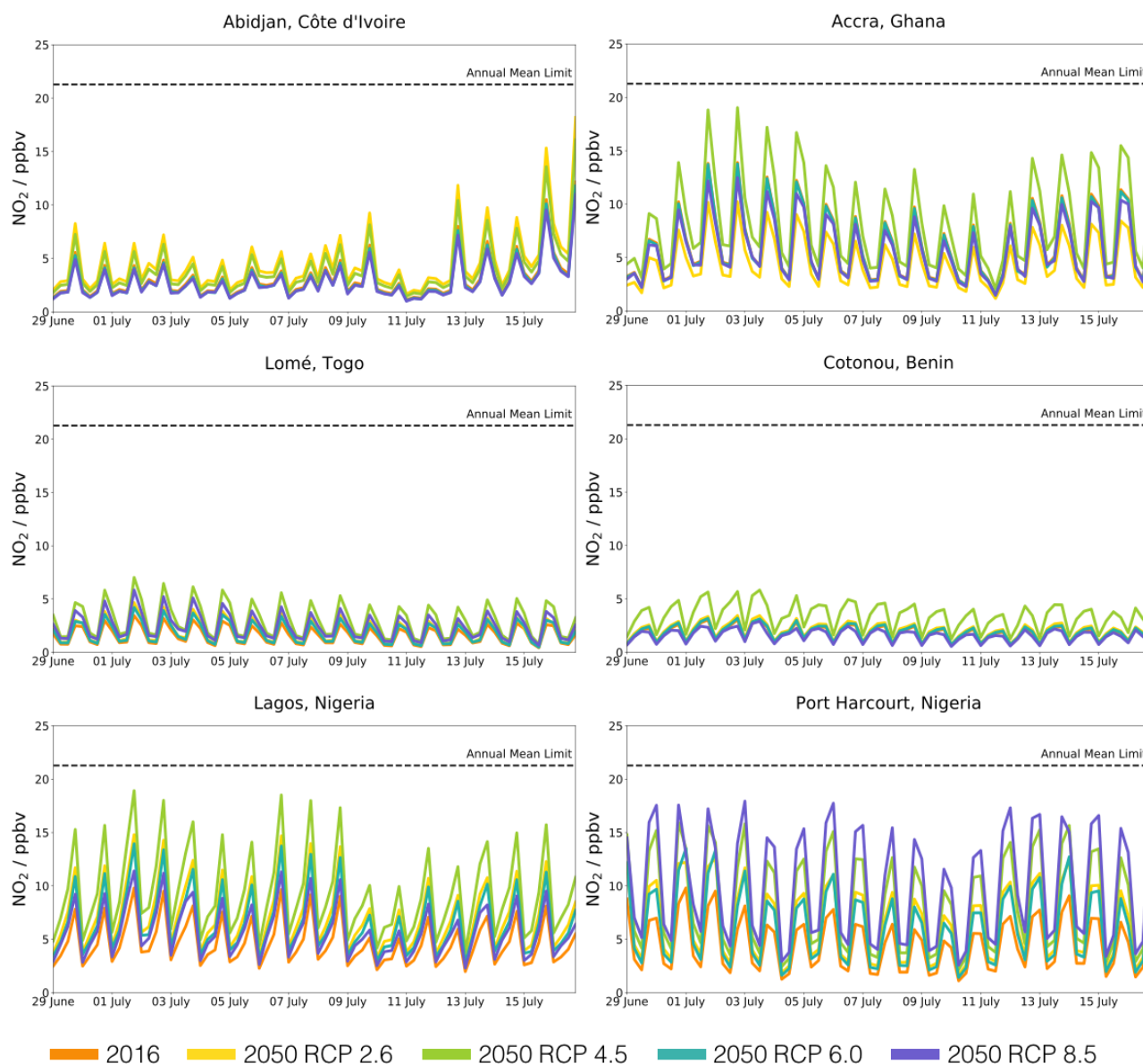
Figure 4.12: Variations in NO$_2$ concentrations over time for the DACCIWA aircraft campaign period for six of the West African coastal cities. This plot compares the model output for 2016 and for each RCP scenario for 2050. The coloured lines show the 6-hour mean concentrations from each of the simulations. The WHO annual mean limit (40 µg m^{-3}, equivalent to ~ 21.3 ppbv) guideline is indicated by the black dashed line.

4.4 Conclusions

We have evaluated a range of potential scenarios for air pollution in West Africa in 2050 based on the predictions of the IPCC RCP scenarios. This evaluation has not considered the impact of changing meteorology for this period or the impact of increasing CH$_4$ concentrations.

We find that the different RCP predictions for southern West Africa are fairly different between the RCPs, between the pollutants and between the key cities. Emissions associated with RCP8.5 which represents that largest climate forcing does not represent the largest change in pollutants.

In general, the results from the model coupled to the emissions suggest that the concentration of pollutants will not change enormously for the DACCIWA cities between 2016 and 2050. Increases or decreases of around 20% - 50% are forecast depending upon the economic pathway used for the RCP. The air quality problem does not appear to get significantly worse for these cities. This likely

reflects a balance between increasing populations and a movement towards the use of technologies which are less environmentally damaging (such as moving from solid to liquid and gaseous fuels).

The situation over Nigeria is less benevolent with some of the scenarios showing substantial increases in the $PM_{2.5}$ concentration over cities such as Lagos and Port Harcourt. However, our understanding of the 2016 scenario is much less well developed for these cities as the DACCIWA project can provide little or no constraint for the conditions here.

5   ETHZ

5.1   5.1 The global aerosol climate model ECHAM6-HAM2

The ECHAM6-HAM2 model is a global aerosol climate model. ECAHM6 is the sixth generation of the atmospheric general circulation model ECHAM. It is described in detail in Stevens et al. (2013). The aerosol module HAM was first implemented in the 5th generation of ECHAM (ECHAM5; Roeckner et al., 2003) by the Max Planck Institute for Meteorology (Stier et al., 2005). Over the past years, the HAM module has been improved and completed with new processes (HAM2) as described in Zhang et al. (2012). The HAM2 module is now coupled to the ECHAM6.

Aerosol microphysics is simulated using the M7 module (Vignati et al., 2004), which accounts for sulfate, black carbon, particulate organic matter, sea salt, and dust. The atmospheric aerosol population is described as a superposition of seven lognormal distributed modes for which standard deviations are prescribed. The total number concentration and masses of the different chemical components are prognostic variables in the model. The modes are divided into soluble, internally mixed modes (containing sulfate) and insoluble, externally mixed modes, which are assigned to different size ranges. The modal diameters can vary and are calculated at each time step from the mass and number concentrations for each mode. Dust particles are considered as part of the soluble and insoluble accumulation and coarse modes. Sedimentation and dry and wet deposition are parameterized as functions of the aerosol size distribution, composition, and mixing state and depend on the ECHAM6 meteorology. The emission fluxes of dust (Tegen et al., 2002, with modifications from Stanelle et al.,2014), seasalt (Long et al., 2011), and dimethyl sulfide from the oceans (DMS) are calculated online, based on the model meteorology. Anthropogenic emissions are prescribed.

For the DACCIWA project we choose to perform model simulations with the recent developed model version ECHAM6.3-HAM2.3. This model version is described and evaluated in Tegen et al. (to be subm.). We performed simulations in T63L47 resolution (approx. 200 km x 200 km horizontal resolution). In the following we will base our analysis on simulations performed in free mode, which means that the large-scale circulation is not prescribed. The model is able to account for feedbacks between aerosols and the atmosphere (via the direct and indirect aerosol effect). But the sea surface temperature (SST) and the sea ice cover (SIC) are prescribed. For present day we use AMIP data (https://pcmdi.llnl.gov/mips/amip/amip2/). But for future conditions we need input from Earth System Models (ESMs). For the 5th phase of the Comprehensive Model Intercomparison Project (CMIP5), different institutes performed a well-defined set of simulations with their ESMs (Taylor et al., 2012). In our study we are interested in the "long term" simulations of twentieth-century climate and projections for the twenty-first century and beyond. But unfortunately, Dunning et al. (2017) show that CMIP5 simulations with coupled ocean-atmosphere models fail in representing the biannual precipitation regime over South West Africa. This misrepresentation is related to a bias in the simulation of the Intertropical Convergence Zone (ITCZ) (Richter and Xie, 2008; Roehrig et al., 2013; Toniazzo and Woolnough, 2014; Monerie et al., 2017), which is connected to the simulation of too warm Atlantic SST in the Gulf of Guinea (Vizy and Cook, 2001; Cook and Vizy, 2006; Roehrig et al.,

2013), via influences on the meridional temperature gradient. Therefore, using the ESM derived SST for future conditions is expected to result in a misrepresentation of the monsoon system. To avoid this problem, we will present future projections which are based on AMIP SST with added change in SST based on the HadGEM2-ESM. We investigate the role of the SST for future projections of aerosol concentration and climate change for Southern West Africa in deliverable 7.5.

In this deliverable our goal is to investigate how the air quality in Southern West Africa could involve until the mid of this century. Thereby we have to keep in mind that our global model has a rather coarse horizontal resolution. This means that the model is not able to capture city plumes. The simulated aerosol concentration reflects a mean over a wider region. Further we will discuss how the radiative forcing of aerosols can change until 2050.

To reach the goals we performed a set of simulations which are summarised in table 5.1. We applied emission inventories developed for the rcp4.5 and rcp8.5 scenarios to the simulations. Further, we applied the rcp8.5 emission inventory for 2050 in a simulation where we used the present-day climate (e.g. trace house gas concentrations, SST, SIC, vegetation cover). To explain our results, we performed an additional simulation where we applied the land cover/ vegetation cover calculated by the MPI-ESM-MR. We will accentuate the need for this simulation later.

5.2 Applied anthropogenic emissions

In the DACCIWA region, indicated by the red box in figure 5.1, all anthropogenic aerosol emissions are expected to increase until 2050 (figure 5.2). The largest increase in emissions is foreseen in the rcp8.5 scenario. The only exception is valid for BC during summertime, where the foreseen emissions are higher in rcp4.5 than in the rcp8.5 scenario. The biomass burning emissions are highest at the Guinea Coast during winter. During Northern-Hemispheric summer the biomass burning emissions occur in central Africa, from there, the biomass burning aerosols are transported to the Guinea Coast.

Table 5.1: Simulations performed with the global aerosol-climate model ECHAM6-HAM2.

Abbreviation	Anthropogenic and biomass burning emissions	Land cover
PD	2010, ACCMIP rcp4.5	PD, based on satellite measurements
PD FUaccmip	2050, ACCMIP rcp8.5	PD, based on satellite measurements
PD cmip5LC	2010, ACCMIP rcp4.5	PD, based on MPI-ESM-MR output
FU rcp8.5	2050, ACCMIP rcp8.5	FU, based on MPI-ESM-MR output rcp8.5
FU rcp4.5	2050, ACCMIP rcp4.5	FU, based on MPI-ESM-MR output rcp4.5

Figure 5.1: West Africa, the boxes indicate regions for those we calculated spatial averages (see figure 5.1). In red, the so called DACCIWA region is indicated.

Figure 5.2: Monthly emission fluxes for different species averaged over black box for anthropogenic plus biomass burning aerosols, and over green box for only biomass burning aerosols respectively. Blue lines indicate fluxes for 2010 and are applied in simulations PD and PD cmip5LC; red lines are applied in the future projection FU rcp8.5, yellow lines in FU rcp4.5 (year 2050).

5.3 Aerosol concentrations

Twenty-year monthly averages of the vertical aerosol profile in the DACCIWA region are shown in figure 6.3. The anthropogenic aerosol concentrations in PD (dark blue lines in figure 5.3) and PD_cmip5LC (light blue lines in figure 5.3) are, as expected, very similar. In both simulations the same emissions are applied. The seasalt concentrations are a bit higher in PD_cmip5LC due to an increase in wind speed. In simulation PD_cmip5LC we prescribe the vegetation cover in our model based on simulations with the MPI-ESM-LR for present day conditions. In PD the vegetation cover is prescribed by satellite estimates as it is usually done in ECHAM6-HAM2. But for performing future projections we need information of the vegetation cover from ESMs. Therefore, we decided to apply the calculated cover in both, a present-day simulation and future projections. The ESM based vegetation cover assumes the presence of more grasses in the west of the Sahara (figure 5.4). This increases the roughness length which results in a decrease of wind speed and therewith a decrease of dust emissions from the Sahara. Less dust particles are transported into the DACCIWA region (this will be further discussed in the upcoming section). The difference in the presence of dust particles is linked to the changes in sulfate concentrations in our area of interest. Gaseous sulfate may coat mineral dust particles, then they transfer from the insoluble to the soluble mode. The particles are removed faster by wet deposition. Less sulfate is present if more dust particles are available.

Often the implication of future emissions on aerosol concentration and air quality is calculated for the present climate, which means technically prescribe future emissions but present-day climate. To check the reliability of this approach we used the same procedure in simulation PDamip_FUaccmip (green line in figure 5.3). As expected the anthropogenic aerosol concentration are higher in that simulation as in PD and PD_cmip5LC, because the future emission fluxes are expected to be higher than the present ones. The lower concentration of dust aerosols in the DACCIWA region is related to the increase in gaseous sulfate concentrations. More dust particles are coated by gaseous sulfate. The particles in the soluble mode are washed out faster, therefore less dust particles reach the area of interest.
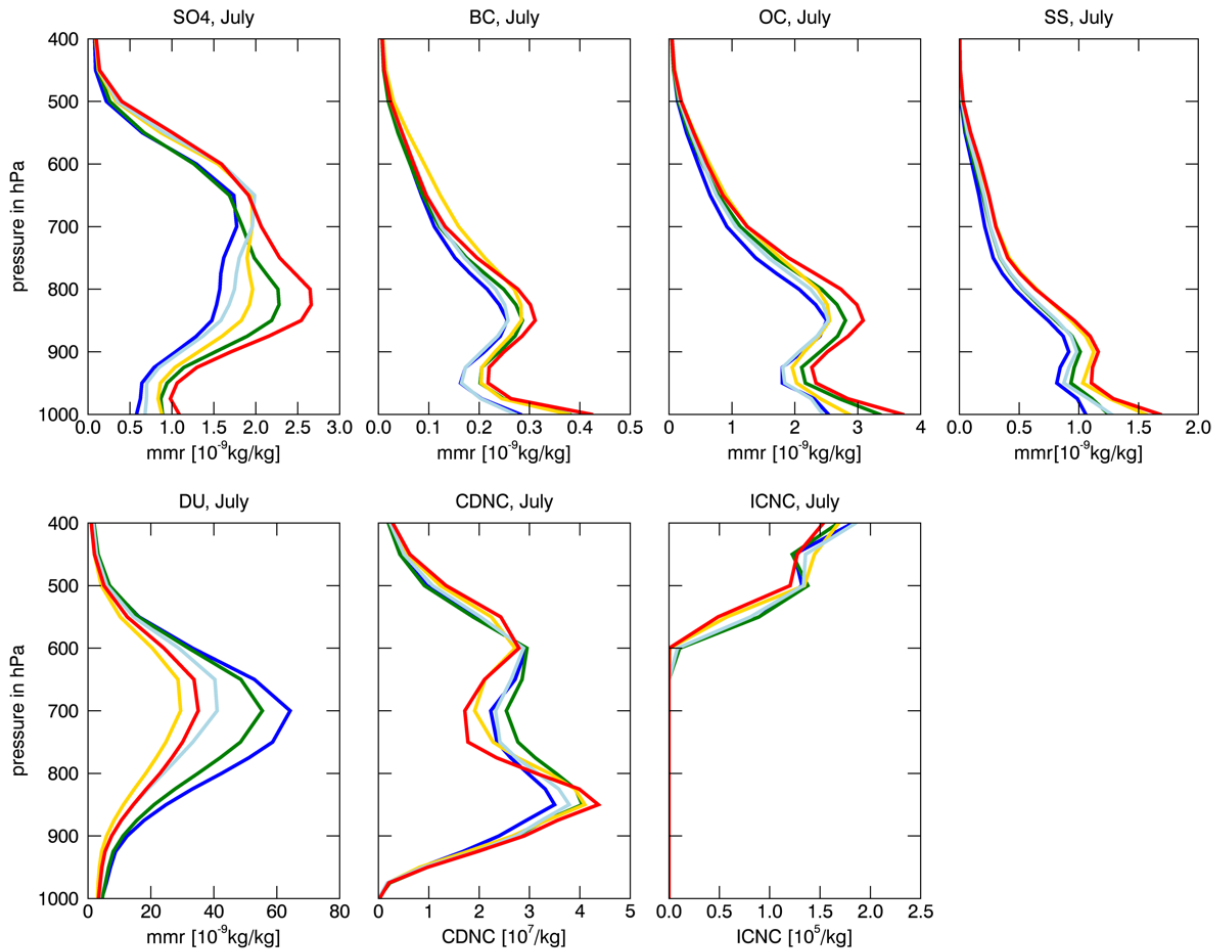
Figure 5.3: Mass mixing ratio for various tracers, Cloud Droplet Number Concentration (CDNC), and Ice Condensation Number Concentration (ICNC) averaged about the "DACCIWA"- box for July. Blue lines indicate concentrations calculated by simulation PD, light blue lines by PD_cmip5LC, green lines by PDamip_FUaccmip, red lines are estimated by future projection FU rcp8.5, yellow lines by FU rcp4.5.

The yellow and red lines in figure 5.4 show the averaged concentrations for July by the mid of the century as calculated by FU rcp4.5 and rcp8.5, respectively. As expected the anthropogenic aerosol concentrations are higher in FU rcp8.5 than in FU rcp4.5. The sea salt concentrations are higher in the future projections than in the present-day simulations because more sea salt particles are emitted if the water is warmer (Long et al., 2011). The dust concentrations are projected to decrease in the future. All present-day simulations estimate higher dust concentrations in the DACCIWA region. The reason therefore is the simulated "Saharan greening" by the MPI-ESM-MR, which is discussed in Bathiany et al. (2014). Due to the CO_2 fertilization effect the vegetation cover is expected to increase in the Sahara until the mid of the century. As discussed above this results in an increase in the roughness length which lowers the wind speed. Dust emissions are proportional to the cubic of the wind speed, therefore a decrease in wind speed lowers the dust emission flux extremely. Additionally, an increase in vegetation lowers the area where dust emissions can take place (availability of potential dust sources). These areas are derived online in our model simulations following the parameterization of Stanelle et al. (2014), where they are calculated in dependency of the applied vegetation cover. The decrease in potential dust sources results also in a decrease of dust emissions in the Sahara. If less dust is emitted, less particles are transported into the DACCIWA region.

Comparing the calculated anthropogenic aerosol concentrations of simulation FU rcp8.5 and PD_FUaccmip with each other, points out that the concentrations are higher in simulation FU rcp8.5, although the same anthropogenic emissions are applied. For SO_4 the reason seems to be again the availability of dust particles (see above). For OC and BC the differences are smaller and seem to be caused by changes in the circulation. This point will be further discussed in deliverable 7.5.
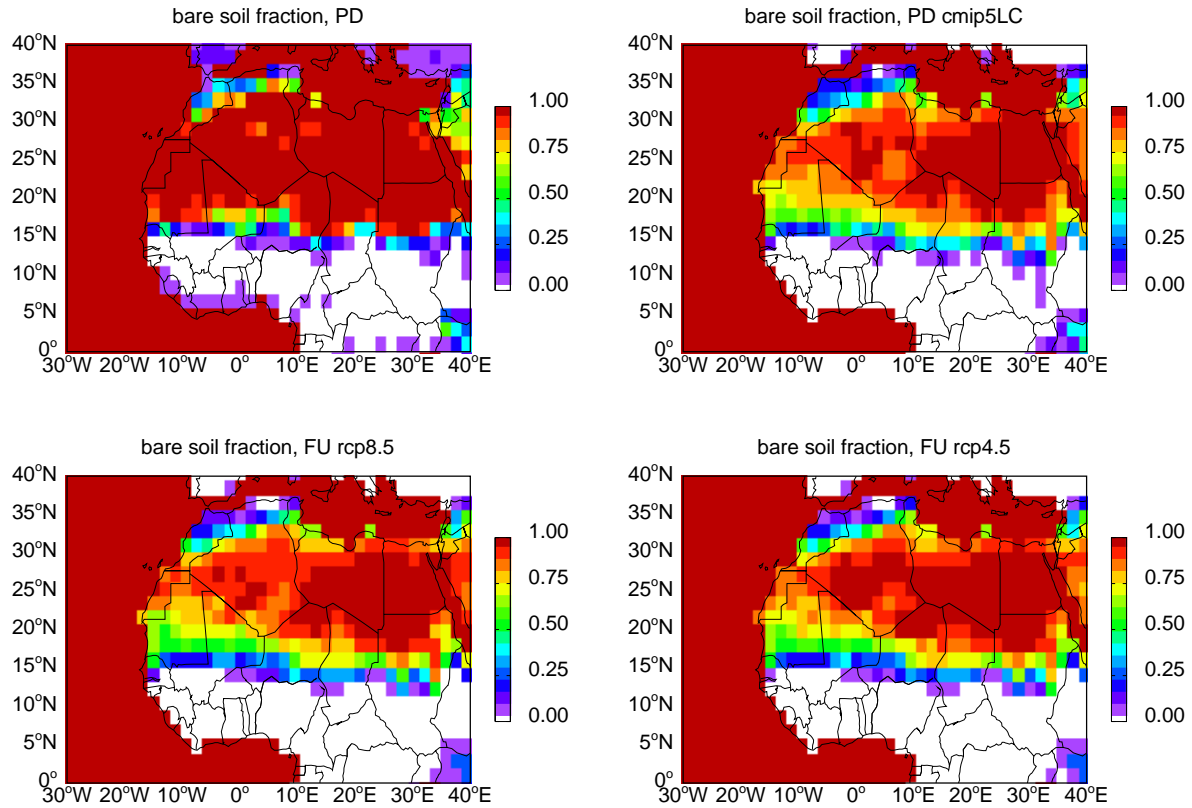

Figure 5.5: Averaged fraction of bare soil per grid cell. The vegetation cover in PD is based on satellite measurements. In simulations PD cmip5LC, FU rcp8.5, and FU rcp4.5 the vegetation cover is based on calculations from the MPI-ESM-MR.

5.4 Air quality

The PM2.5 surface concentration is a good measure in terms of air quality. Small particles can penetrate deeply into the lung and can affect human's health. In the following we will present regional averages for the DACCIWA region. We want to point out that all presented values are only valid as averaged values. With the rather coarse model resolution of approximately 200 km x 200 km our model is not able to resolve cities. Therefore, we have to assume that PM2.5 concentration inside the populated cities are even higher and therewith the risk of respiratory infections, townspeople are exposed to, should be even larger. In 2005 the World Health Organization (WHO) gave guidelines of appropriate PM2.5 concentrations: 10 µg/m^3 as annual mean and 25 µg/m^3 as daily mean.

Table 5.2: Multi-annual mean value of PM2.5 surface concentrations averaged over the "DACCIWA" region as simulated by ECHAM6-HAM2.

	PM2.5 surface concentration	PM1 surface concentration
PD	44.1 µg/m^3	32.5 µg/m^3
PD cmip5LC	18.8 µg/m^3	14.9 µg/m^3
PD FUaccmip	44.1 µg/m^3	33.0 µg/m^3
FU rcp8.5	16.5 µg/m^3	13.8 µg/m^3
FU rcp4.5	14.0 µg/m^3	11.7 µg/m^3

In table 5.2 the multi-annual mean PM2.5 surface presentations calculated by our different model runs are presented. It is obvious that the recommended annual limit of 10 µg/m^3 is overshot in all scenarios. This is particularly alarming in regard of the fact that we have to assume that the concentrations inside the cities are even higher. The main reason for the high PM2.5 and also PM1 values is caused by the presence of dust particles in our area of interest (figure 5.6). This is especially true during winter time when the seasonal averaged concentration is above 75 µg/m^3 (estimated in simulation PD with the application of satellite-based vegetation cover). Assuming that the presence of grass in the Sahara is underestimated in the satellite derived vegetation cover, which is not very likely, the PM2.5 concentration is still at a high level (above 25 µg/m^3). This points out that dust particles are the main contributor to the PM2.5 load in the DACCIWA region during winter.

As we already discussed in the last section, the presence of dust is projected to decrease until the mid of the century. The reason is given by the simulated Saharan greening by the MPI Earth System Model. This decrease in dust concentration overcompensates the increase in anthropogenic aerosols in the area of interest during winter. The PM2.5 as well as the PM1 surface concentrations are expected to decrease until 2050. But as there is a large derivation between simulated and satellite-based vegetation cover for present day conditions, this result has to be taken with care. During summer the increase in anthropogenic aerosol concentrations has more negative effects to the air quality at the mid of the century.
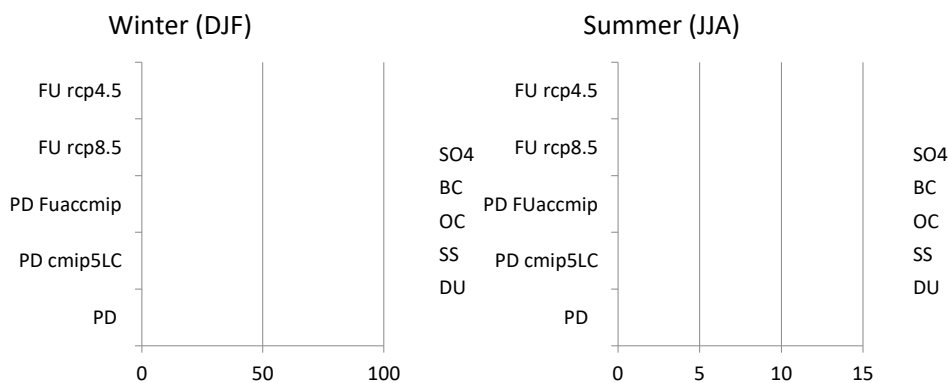

Figure 5.6: Multi-seasonal mean PM2.5 surface concentration in µg/m^3 averaged over "DACCIWA" region, which is indicated as red box in figure 5.1.

5.5   Radiative forcing

The aerosol radiative forcing is calculated by a double call to the radiation routine in ECHAM6-HAM2. Ones the radiation routine is called with aerosol calculated properties included, ones without them. In the remainder of the section, we refer to radiative forcing as being the difference between the two calls. Further we focus on the northern hemispheric summer season as the DACCIWA project is designed to do.

For the DACCIWA region, the largest clear sky negative shortwave forcing at both, the surface and top of the atmosphere (top), is simulated by PD FUaccmip, where also the highest aerosol burden is estimated (table 5.3). The longwave forcing is with 1.01 W/m^2 at the surface and 0.57 W/m^2 at top very similar to the calculated forcing in PD (1.03 W/m^2 and 0.59 W/m^2, respectively). Consequently, the lowest aerosol radiative forcing is calculated by the simulation with the lowest aerosol burden, FU amipH rcp4.5.

Table 5.3: Multi-seasonal summer mean clear sky radiative forcing averaged over "DACCIWA" box (SW – shortwave, LW – longwave, sfc – surface, top – top of atmosphere).

	SW sfc	LW sfc	SW top	LW top
PD	-12.91 W/m^2	1.03 W/m^2	-5.41 W/m^2	0.59 W/m^2
PD cmip5LC	-12.24 W/m^2	0.79 W/m^2	-4.9 W/m^2	0.47 W/m^2
PD FUaccmip	-13.58 W/m^2	1.01 W/m^2	-5.68 W/m^2	0.57 W/m^2
FU amipH rcp4.5	-12.2 W/m^2	0.66 W/m^2	-4.68 W/m^2	0.36 W/m^2
FU amipH rcp8.5	-12.67 W/m^2	0.71 W/m^2	-5.28 W/m^2	0.39 W/m^2

The shortwave aerosol radiative forcing estimated in simulation PD is higher (SW sfc: 0.65, LW sfc: 0.24, SW top: 0.51, LW top: 0.12) than in PD cmip5LC. This is caused by the larger amount of dust particles in our region of interest simulated in PD. To avoid the fact that different sources are used for prescribing the vegetation cover, we compare the future projections only with PD cmip5LC. Only the simulation, where the rcp8.5 scenario is applied (FU amipH rcp85), calculates an increase in the radiative forcing until the mid of the century. The net increase is -0.51 W/m^2 at the surface and -0.46 W/m^2 at top. Under scenario rcp4.5 the increase in anthropogenic aerosol concentration can be compensated by a reduction in dust content in our area of interest during summer. Therefore, the radiative forcing is projected to decrease until 2050, which would result in a warming.

5.6   Summary and conclusions

A key role in estimating the aerosol burden in South West Africa, and in particular in the DACCIWA domain, is to understand the dust emissions in the Sahara and their transport to the coast. During winter the regional aerosol burden is dominated by dust particles which are transported from the Sahara to the coast. The PM2.5 surface concentration is with 25 – 75 µg/m^3 (depending of the applied vegetation cover) quite high in present day conditions. Anthropogenic aerosol emissions are expected to increase in SWA until 2050. This increase in anthropogenic emissions can be overcompensated by a reduction in the amount of dust particles affecting our area of interest during winter. This is caused by a greening in the Sahara which is projected by different ESMs (Bathiany et al., 2014). But during summer the anthropogenic contribution to the total aerosol pollution is much larger. The total PM2.5 surface concentrations are with 7 – 9 µg/m^3 significantly lower. The concentration is expected to stay at the same level until 2050 when the rcp8.5 scenario is applied.

This is again a consequence of the compensation of the increase in anthropogenic emission by the reduction in dust particles. But we have to point out that these findings are only valid for regional averaged conditions, in the cities the anthropogenic contribution to the total aerosol load is expected to be much higher.

Without the consideration of future changes in climate and land cover the aerosol load is expected to increase in SWA until 2050 in both, summer and winter season. But the simulated change in anthropogenic aerosols is the same as simulated by FU rcp8.5.

The change in net radiative forcing is -0.51 W/m^2 at the surface and -0.46 W/m^2 at top until the mid of the century when considering the rcp8.5 scenario. This would result in a cooling. If the rcp4.5 scenario is applied a slight warming is simulated.

6 Final remarks and conclusions

This report consists of four studies within the DACCIWA project with each of them addressing the question about the impact of changing aerosol and gas emissions on the climate and air quality in Southern West Africa until the mid of the century. Three groups performed simulations with their model system applying approximations for future emissions which are based on the IPCC RCPs. The research group of UoY added the estimated change of emission fluxes based on the different RCPs to the present-day emission fluxes developed in the DACCIWA project. Therefore, the change in emissions between PD and 2050 is the same as in simulations preformed with the global aerosol climate model ECHAM6-HAM2. But the emissions themselves differ between each other. The present-day simulation performed with the WRF-CHIMERE model considers the HTAP emission inventory. So, the change between present day and future emission fluxes is different to the change applied to the other models.

The present-day simulations suggest that the DACCIWA region is already today affected by a very high concentrations of PM2.5. The WHO recommendations of a limit in PM2.5 surface concentration of 25 µg/m^3 as 24 h – average and 10 µg/m^3 as annual mean is clearly overshot. In particular, this is true during winter season when the DACCIWA region is affected by transported dust particles which are emitted in the Sahara. But also, during summer, when the anthropogenic contribution to the PM2.5 concentration is larger as the natural one, the limits are reached in populated areas. For gases, the situation is different. The models do not simulate an exceeding of the recommended limits for neither ozone (100 µg/m^3 as 8h average) nor NO$_2$ (annual mean value of 40 µg/m^3)

All models simulate an increase in PM2.5 surface concentrations when the rcp8.5 scenario is applied. The concentrations of O$_3$ and NO$_2$ are simulated to only increase slightly. The increase is more pronounced for large cities, especially for Lagos and Port Harcourt in Nigeria. For other cities in the DACCIWA region it can be suggested that the concentration of pollutants will not change dramatically. The air quality problem does not appear to get much worse for these cities. This likely reflects a balance between increasing populations and a movement towards the use of technologies which are less environmentally damaging (such as moving from solid to liquid and gaseous fuels).

If considering a change in climate and vegetation cover due to increase in trace gas concentrations the situation seems to be even more recreational. The expected increase in anthropogenic aerosol concentrations is then compensated by a reduction in dust concentrations in the DACCIWA region. But we have to keep in mind that the reason for the reduction in dust concentration, the Saharan greening, is simulated by different Earth System Models. But there is no guaranty that this will be fulfilled. And even if the Saharan greening will become true, the PM2.5 levels are already very high.

The people living in cities in South West Africa are exposed to high health risks. They would benefit if anthropogenic emissions will not increase.

The aerosols can affect the climate via direct and indirect effects. The net radiative forcing at the surface and the top of the atmosphere is expected to increase (get more negative). This would result in a cooling. The change in the radiative budget in Southern West Africa is hypothesized to have consequences for dynamical feature as the Atlantic Inflow and could feedback with the presence of clouds.

References

KIT

Athanasopoulou, E., Vogel, H., Vogel, B., Tsimpidi, A. P., Pandis, S. N., Knote, C., and Fountoukis, C.: Modeling the meteorological and chemical effects of secondary organic aerosols during an EUCAARI campaign, Atmos. Chem. Phys., 13, 625–645, 2013.

Baldauf, M., Seifert, A., Förstner, J., Majewski, D., and Raschendorfer, M.: Operational Convective-Scale Numerical Weather Prediction with the COSMO model: Description and Sensitivities, Mon. Wea. Rev., pp. 3887–3905, 2011.

CAMS: Copernicus Atmosphere Monitoring Service (http://apps.ecmwf.int/ datasets/data/cams-gfas/, last access: 30 July 2017), 2017.

CCSM: https://svn-ccsm-inputdata.cgd.ucar.edu/trunk/inputdata/lnd/clm2/raw data/pftlanduse.3minx3min.simyr2000.c110 913/ (last access: 10 June 2017), 2015.

Deetz, K. and Vogel, B.: Development of a new gas-flaring emission dataset for southern West Africa, Geosci. Model Dev., 10, 1607–1620, 2017.

EDGAR: Emission Database for Global Atmospheric Research, http://edgar.jrc.ec.europa.eu/htap_v2/index.php?SECURE=123 (last access: 10 June 2017), 2010.

Fountoukis, C. and Nenes, A.: Continued development of a cloud droplet formation parameterization for global climate models, J. Geophys. Res., 110, 2005.

Fountoukis, C. and Nenes, A.: ISORROPIA II: a computationally efficient thermodynamic equilibrium model for K^+-Ca^{2+}-Mg^{2+} NH_4^+-$SO_4^{2-}$$NO_3^-$$CL^-$-$H_2O$ aerosol, Atmos. Chem. Phys., 7, 4639–4659, 2007.

GlobCover: GlobCover Land Cover Map - European Space Agency GlobCover Project (http://www.gelib.com/globcover-2009.htm, last access: 10 June 2017), 2009.

Grams, C. M., Jones, S. C., Marsham, J. H., Parker, D. J., Haywood, J. M., and Heuveline, V.: The Atlantic Inflow to the Saharan heat low: Observations and Modelling, Quart. J. Roy. Meteor. Soc., 136, 125–140, 2010.

HWSD: HWSD (FAO/IIASA/ISRIC/ISSCAS/JRC), 2012: Harmonized World Soil Database (version 1.2), FAO, Rome, Italy and IIASA, Laxenburg, Austria, 2012.

Kalthoff, N., Louhou, F., Brooks, B., Jegede, O., Adler, B., Babi´c, K., Dione, C., Ajao, A., Amekudzi, L. K., Aryee, J. N. A., Bessardon, G., Danuor, S. K., Handwerker, J., Kohler, M., Lothon, M., Pedruzo-Bagazgoitia, X., Smith, V., Sunmonu, L., Wieser, A., Fink, A. H., and Knippertz, P.: The diurnal cycle of the southern West African atmospheric boundary layer during the DACCIWA campaign, Atmos. Chem. Phys., under review, 2017.

Knippertz, P., Fink, A. H., Deroubaix, A., Morris, E., Tocquer, F., Evans, M. J., Flamant, C., Gaetani, M., Lavaysse, C., Mari, C., Marsham, J. H., Meynadier, R., Affo-Dogo, A., Bahaga, T., Brosse, F., Deetz, K., Guebsi, R., Latifou, I., Maranan, M., Rosenberg, P. D., and Schlüter, A.: A meteorological and chemical overview of the DACCIWA field campaign in West Africa in June-July 2016, Atmos. Chem. Phys., pp. 10 893–10 918, 2017.

Lundgren, K., Vogel, B., Vogel, H., and Kottmeier, C.: Direct radiative effects of sea salt for the Mediterranean region under conditions of low to moderate wind speeds, J. Geophys. Res., 118, 1906–1923, 2013.

Lana, A., Bell, T. G., Simó, R., Vallina, S. M., Ballabrera-Poy, J., Kettle, A. J., Dachs, J., Bopp, L., Saltzman, E. S., Stefels., J., Johnson, J. E., and Liss, P. S.: An updated climatology of surface dimethylsulfide concentrations and emission fluxes in the global ocean, Global Biogeochem. Cycles, 25, G1004, 2011.

MOZART: MOZART-4/GEOS-5 forecasts, National Center for Atmospheric Research (NCAR), University Corporation for Atmospheric Research, Atmospheric Chemistry Observations & Modeling (https://www.acom.ucar.edu/acresp/AMADEUS/ mz4_output/chemfcst/, last access: 30 July 2017), 2017.

Philipps, V. T. J., DeMott, P. J., and Andronache, C.: An Empirical Parameterization of Heterogeneous Ice Nucleation for Multiple Chemical Species of Aerosol, J. Atmos. Sci., 65, 2757–2783, 2008.

Rieger, D., Steiner, A., Bachmann, V., Gasch, P., Förstner, J., Deetz, K., Vogel, B., and Vogel, H.: Impact of a Saharan dust outbreak on the photovoltaic power generation in Germany, Atmos. Chem. Phys., 17, 13 391–13 415, 2017.

Riemer, N., Vogel, H., Vogel, B., and Fiedler, F.: Modeling aerosols of the mesoscale-y: Treatment of soot aerosols and its radiative effects, J. Geophys. Res., 108, 2003.

Schuster, R., Fink, A. H., and Knippertz, P.: Formation and Maintenance of Nocturnal Low-Level Stratus over the Southern West African Monsoon Region during AMMA 2006, J. Atmos. Sci., 70, 2337–2355, 2013.

Seifert, A. and Beheng, K. D.: A two-moment cloud microphysics parameterization for mixed-phase clouds. Part 1: Model description, Meteor. Atmos. Phys., 92, 45–66, 2006.

Vogel, B., Vogel, H., Bangert, M., Lundgren, K., Rinke, R., and Stanelle, T.: The comprehensive model system COSMO-ART – Radiative impact of aerosol on the state of the atmosphere on the regional scale, Atmos. Chem. Phys., 9, 8661–8680, 2009.

Walter, C., Freitas, S. R., Kottmeier, C., Kraut, I., Rieger, D., Vogel, H., and Vogel, B.: The importance of plume rise on the concentrations and atmospheric impacts of biomass burning aerosol, Atmos. Chem. Phys., 16, 9201–9219, 2016.

Weimer, M., Schröter, J., Eckstein, J., Deetz, K., Neumaier, M., Fischbeck, G., Hu, L., Millet, D. B., Rieger, D., Vogel, H., Vogel, B., Reddmann, T., Kirner, O., Ruhnke, R., and Braesicke, P.: An emission module for ICON-ART 2.0: implementation and simulations of acetone, Geosci. Model Dev., 10, 2471–2494, 2017.

UPMC

Menut, L., Bessagnet, B., Khvorostyanov, D., Beekmann, M., Blond, N., Colette, A., Coll, I., Curci, G., Foret, G., Hodzic, A., Mailler, S., Meleux, F., Monge, J.-L., Pison, I., Siour, G., Turquety, S., Valari, M., Vautard, R., and Vivanco, M. G.: CHIMERE 2013: a model for regional atmospheric composition modelling, Geosci. Model Dev., 6, 981-1028, https://doi.org/10.5194/gmd-6-981-2013, 2013a.

Mailler S., L. Menut, D. Khvorostyanov, M. Valari, F. Couvidat, G. Siour, S. Turquety, R. Briant, P. Tuccella, B. Bessagnet, A. Colette, L. Letinois, and F. Meleux, 2017, CHIMERE-2017: from urban to hemispheric chemistry-transport modeling , Geosci. Model Dev., 10, 2397-2423, https://doi.org/10.5194/gmd-10-2397-2017, 2017

Bian, H. and Prather, M.: Fast-J2: accurate simulation of stratospheric photolysis in global chemical models, J. Atmos. Chem., 41, 281-296, 2002.

Hauglustaine, D. A. and Balkanski, Y. and Schulz, M., 2014, A global model simulation of present and future nitrate aerosols and their direct radiative forcing of climate, Atm. Chem. Phys. 14, 6863-6949, 10.5194/acpd-14-6863-2014.

Ginoux, P., Chin, M., Tegen, I., Prospero, J. M., Holben, B., Dubovik, O., and Lin, S. J.: Sources and distributions of dust aerosols simulated with the GOCART model, J. Geophys. Res., 106, 20255-20273, 2001.

Janssens-Maenhout, G. and Crippa, M. and Guizzardi, D. and Dentener, F. and Muntean, M. and Pouliot, G. and Keating, T. and Zhang, Q. and Kurokawa, J. and Wankmuller, R. and Denier van der Gon, H. and Kuenen, J. J. P. and Klimont, Z. and Frost, G. and Darras, S. and Koffi, B. and Li, M., 2015, HTAP v2.2: a

mosaic of regional and global emission grid maps for 2008 and 2010 to study hemispheric transport of air pollution, Atmospheric Chemistry and Physics, 15, 11411--11432, 10.5194/acp-15-11411-2015.

Wild, O., Zhu, X., and Prather, J.: Fast-J: accurate simulation of the in- and below-cloud photolysis in tropospheric chemical models, J. Atmos. Chem., 37, 245–282, 2000

UoY

Alexander, B., Park, R. J., Jacob, D. J., Li, Q. B., Yantosca, R. M., Savarino, J., … Thiemens, M. H. (2005). Sulfate formation in sea-salt aerosols: Constraints from oxygen isotopes. *Journal of Geophysical Research*, *110*(D10), D10307. https://doi.org/10.1029/2004JD005659

Bey, I., Jacob, D. J., Yantosca, R. M., Logan, J. A., Field, B. D., Fiore, A. M., … Schultz, M. G. (2001). Global modeling of tropospheric chemistry with assimilated meteorology: Model description and evaluation. *Journal of Geophysical Research*, *106095*(16), 73–23. https://doi.org/10.1029/2001JD000807

Breider, T. J., Mickley, L. J., Jacob, D. J., Ge, C., Wang, J., Payer Sulprizio, M., … Hopke, P. K. (2017). Multidecadal trends in aerosol radiative forcing over the Arctic: Contribution of changes in anthropogenic aerosol to Arctic warming since 1980. *Journal of Geophysical Research: Atmospheres*, *122*(6), 3573–3594. https://doi.org/10.1002/2016JD025321

Clarke, L., Edmonds, J., Jacoby, H., Pitcher, H., Reilly, J., Richels, R. (2007). Scenarios of Greenhouse Gas Emissions and Atmospheric Concentrations. Sub-report 2.1A of Synthesis and Assessment Product 2.1 by the U.S. Climate Change Science Program and the Subcommittee on Global Change Research. Department of Energy, Office of Biological & Environmental Research, Washington, 7 DC., USA, 154 pp.

Fujino, J., Nair, R., Kainuma, M., Masui, T., Matsuoka, Y., (2006). Multi-gas mitigation analysis on stabilization scenarios using AIM global model. Multigas Mitigation and Climate Policy. The Energy Journal Special Issue.

Guenther, A. B., Jiang, X., Heald, C. L., Sakulyanontvittaya, T., Duhl, T., Emmons, L. K., & Wang, X. (2012). The Model of Emissions of Gases and Aerosols from Nature version 2.1 (MEGAN2.1): an extended and updated framework for modeling biogenic emissions. *Geoscientific Model Development*, *5*(6), 1471–1492. https://doi.org/10.5194/gmd-5-1471-2012

Hijioka, Y., Matsuoka, Y., Nishimoto, H., Masui, M., Kainuma, M., (2008). Global GHG emissions scenarios under GHG concentration stabilization targets. Journal of Global Environmental Engineering 13, 97-108.

Hudman, R. C., Moore, N. E., Mebust, A. K., Martin, R. V., Russell, A. R., Valin, L. C., & Cohen, R. C. (2012). Steps towards a mechanistic model of global soil nitric oxide emissions: implementation and space based-constraints. *Atmospheric Chemistry and Physics*, *12*(16), 7779–7795. https://doi.org/10.5194/acp-12-7779-2012

Jaeglé, L., Quinn, P. K., Bates, T. S., Alexander, B., & Lin, J.-T. (2011). Global distribution of sea salt aerosols: new constraints from in situ and remote sensing observations. *Atmospheric Chemistry and Physics*, *11*(7), 3137–3157. https://doi.org/10.5194/acp-11-3137-2011

Junker, C., & Liousse, C. (2008). A global emission inventory of carbonaceous aerosol from historic records of fossil fuel and biofuel consumption for the period 1860;1997. *Atmospheric Chemistry and Physics*, *8*(5), 1195–1207. https://doi.org/10.5194/acp-8-1195-2008

Kaiser, J. W., Flemming, J., Schultz, M. G., Suttie, M., Wooster, M. J. (2009) The MACC Global Fire Assimilation System: First Emission Products (GFASv0), Tech. Memo. 596, ECMWF, Reading, UK

Kaiser, J. W., Heil, A., Andreae, M. O., Benedetti, A., Chubarova, N., Jones, L., … van der Werf, G. R. (2012). Biomass burning emissions estimated with a global fire assimilation system based on observed fire radiative power. *Biogeosciences*, *9*(1), 527–554. https://doi.org/10.5194/bg-9-527-2012

Murray, L. T., Jacob, D. J., Logan, J. A., Hudman, R. C., & Koshak, W. J. (2012). Optimized regional and interannual variability of lightning in a global chemical transport model constrained by LIS/OTD satellite data. *Journal of
Geophysical Research: Atmospheres*,
117(D20). https://doi.org/10.1029/2012JD017934

Riahi, K., Grübler, A., & Nakicenovic, N. (2007). Scenarios of long-term socio-economic and environmental development under climate stabilization. *Technological Forecasting and Social Change*, *74*(7), 887–935. https://doi.org/10.1016/j.techfore.2006.05.026

Smith, S. J. and Wigley, T. M. L. (2006). Multi-Gas Forcing Stabilization with the MiniCAM. Energy Journal (Special Issue #3) pp 373-391.

van Vuuren, D. P., den Elzen, M. G. J., Lucas, P. L., Eickhout, B., Strengers, B. J., van Ruijven, B., Wonink, S., van Houdt, R. (2007). Stabilizing greenhouse gas concentrations at low levels: an assessment of reduction strategies and costs. *Climatic Change*, *81*(2), 119–159. https://doi.org/10.1007/s10584-006-9172

Wise, M. A., Calvin, K. V., Thomson, A. M., Clarke, L. E., Bond-Lamberty, B., Sands, R. D., Smith, S. J., Janetos, A. C., Edmonds, J. A. (2009). Implications of Limiting CO2 Concentrations for Land Use and Energy. Science. 324:1183-1186. May 29, 2009.

Zender, C. S., Bian, H., & Newman, D. (2003a). Mineral Dust Entrainment and Deposition (DEAD) model: Description and 1990s dust climatology. *Journal of
Geophysical Research*, *108*(D14),
4416. https://doi.org/10.1029/2002JD002775

Zender, C. S., Newman, D., & Torres, O. (2003b). Spatial heterogeneity in aeolian erodibility: Uniform, topographic, geomorphic, and hydrologic hypotheses. *Journal of Geophysical Research*, *108*(D17), 4543. https://doi.org/10.1029/2

ETHZ

Bathiany, S., Claussen, M., and Brovkin, V. (2014). CO2-Induced Sahel Greening in three CMIP5 Earth System Models, J. of Climate, 27, 7163-7184, doi:10.1175/JCLI-D-13-00528.1.

Cheng, T., Peng, Y., Feichter, J., and Tegen, I. (2008). An improvement on the dust emission scheme in the global aerosol-climate model ECHAM5-HAM. *Atmos. Chem. Phys., 8*, 1105-1117.

Cook, K. H. and Vizy, E. K. (2006). Coupled model simulations of the West African monsoon system: twentieth- and twenty-first-century simulations. *J. Clim., 19*, 3681-3703.

Dunning, C. M., Allan, R. P., and Black, E. (2017). Identification of deficiencies in seasonal rainfall simulated by CMIP5 climate models. *Environm. Res. Letters, 12*(11114001).

Lamarque, J.-F. and T. C. Bond and V. Eyrin and C. Granier and A. Heil and Z. Klimont and D. Lee and C. Liousse and A. Mieville and B. Owen and M. G. Schultz and D. Shindell and S. J. Smith and E. Stehfest and J. Van Aardenne and O. R. Cooper and M. Kainu. (2010). Historical (1850-2000) gridded anthropogenic and biomass burning emissions of reactive gases and aerosols: methodology and application. *Atmos. Chem. Phys., 10*, 7017-7039.

Lohmann, U., Stier, P., Hoose, C., Ferrachat, S., Kloster, S., Roeckner, E., and Zhang, J. (2007). Cloud microphysics and aerosol indirect effects in the global climate model ECHAM5-HAM. *Atmos. Chem. Phys., 7*, 3425-3446.

Long, M. S., Kenne, W. C., Kieber, D. J., Erickson, D. J., and Marina, H. (2011). A sea-state based source function for size- and composition-resolved marine aerosol production. *Atmos. Chem. Phys., 11*, 1203-1216.

Monerie, P. A., Sanchez-Gomez, E., and Boé, J. (2017). On the range of future Sahel precipitation projections and the selection of a sub-sample of CMIP5 models for impact studie. *Clim. Dyn., 48*, 2751-2770.

Richter, I., and Xie, S. P. (2008). On the origin of equatorial Atlantic biases in coupled general circulation models. *Clim. Dyn., 31*, 587-598.

Roeckner, E., G.Baeuml, L. Bonventura, R. Brokopf, M. Esch, M. Giorgetta, S. Hagemann, I. Kirchner, L. Kornblueh, E. Manzini, U. Rhodin, U. Schlese, U. Schulzweida, A. Tomkins, 2003: The atmospheric general circulation model ECHAM5. Part I: Model description, Report 349, Max Planck Institute for Meteorology, Hamburg, Germany.

Roehrig, R., Bouniol, D., Guichard, D., Hourdin, F., and Redelsperger, J. L. (2013). The present and future of the West African monsoon: a process-oriented assessment of CMIP5 simulations along the AMMA transect. *J. Clim., 26*, 6471-6505.

Stanelle, T., Bey, I., Raddatz, T., Reick, C., and Tegen, I. (2014). Anthropogenically induced changes in twentieth century mineral dust burden and the associated impact on radiative forcing. *J. Geophys. Res., 119*, 13,526-13,546.

Stevens, B., Giorgetta, M., Esch, M., Mauritsen, T., Crueger, T., Rast, S., Salzmann, M., Schmidt, H., Bader, J., Block, K., Brokopf, R., Fast, I., Kinne, S., Kornblueh, L., Lohmann, U., Pincus, R., Reichler, T., and Roeckner, E. (2013). Atmospheric component of the MPI-M Earth System Model: ECHAM6. *J. Adv. Model. Earth Syst., 5*, 146-172.

Stier, P., Feichter, J., Kinne, S., Kloster, S., Vignati, E., Wilson, J., Ganzeveld, L., Tegen, I., Werner, M., Balkanski, Y., Schulz, M. Boucher, O., Minikin, A., Petzold, A. (2005). The aerosol-climate model ECHAM5-HAM. *Atmos. Chem. Phys., 5*, 1125-1156.

Taylor, K. E., Stouffer, R. J., and Meehl, G. A. (2012). An Overview of CMIP5 and the Experiment Design. *BAMS*, 485-498.

Tegen, I., Harrison, S. P., Kohfeld, K., Prentice, I. C., Coe, M., and Heimann, M. (2002). Impact of vegetation and preferential source areas on global dust aerosol: Results from a model study. *J. Geophys. Res., 107*, D21.

Tegen, I., Lohmann, U., Neubauer, D., Siegenthaler-Le Drian, C., Ferrachat, S., Bey, I., Stanelle, T., Frontoso, G., Stier, P., Schutgens, N., Schmidt, H., Rast, S., Kokkola, H., Barthel, S., and Heinold, B. (to be subm.), The aerosol-climate model ECHAM6.3-HAM2.3: Aerosol evaluation.

Toniazzo, T. and Woolnough, S. (2014). Development of warm SST errors in the southern tropical Atlantic in CMIP5 decadal hindcasts. *Clim. Dyn., 43*, 2889.

Vignati, E., Wilson, J., and Stier, P. (2004). M7: An efficient size-resolved aerosol microphysics module for large-scale aerosol transport models. *J. Geophys. Res., 109*, D22.

Vizy, E. K. and Cook, K. H. (2001). Mechanisms by which Gulf of Guinea and eastern North Atlantic sea surface temperature anomalies can influence African rainfall. *J. Clim., 14*, 795-821.

Zhang, K., O'Donnell, D., Kazil, J., Stier, P., Kinne, S., Lohmann, U., Ferrachat, S., Croft, B., Quaas, J., Wam, H, Rast, S., and Feichter, J. (2012). The global aerosol-climate model ECHAM-HAM, version 2: Sensitivity to improvements in process representations. *Atmos. Chem. Phys, 12*, 8911-8949.